JOURNAL OF COMPUTATIONAL PHYSICS **127,** 424–451 (1996)
ARTICLE NO. 0185

Numerical Simulation of a Thermoacoustic Refrigerator

I. Unsteady Adiabatic Flow around the Stack

ANIRUDDHA S. WORLIKAR AND OMAR M. KNIO

Department of Mechanical Engineering, The Johns Hopkins University, Baltimore, Maryland 21218-2686

Received June 16, 1995; revised January 30, 1996

A low Mach-number compressible flow model for the simulation of acoustically driven flow in a thermoacoustic stack is constructed. The model is based on the assumption that the acoustic wavelength is much larger than the characteristic hydrodynamic lengthscale. Thus, a simplified description of the flow is obtained which still retains the essential features of acoustically induced velocity oscillations near solid boundaries. A vorticity-based formulation of the governing equation is derived which relies on the Helmholtz decomposition of the velocity vector into irrotational and divergence-free components. Irrotational motion is used to represent the action of acoustic waves. Meanwhile the divergence-free velocity component is used to capture the nonlinear vortical perturbations due to no-slip boundaries. A simplified version of the model is applied to analyze unsteady flow in the neighborhood of an idealized thermoacoustic stack which consists of a periodic array of thin plates placed in an acoustic standing wave. Computed results are used to analyze, for different stack configurations, the nonlinear response of the flow to different acoustic driving amplitudes and frequencies. In particular, it is shown that the flow is dominated by the motion of vortices which result from the shedding of boundary layers from the edges of the stack. The dependence of energy losses on stack configuration and operating conditions is also examined.

1. INTRODUCTION

In its simplest form, a thermoacoustic refrigerator essentially consists of a straight resonance tube and a stack of parallel plates (Fig. 1). By exciting a standing wave within the resonance tube, a temperature gradient develops across the stack, thereby enabling heat exchange between two systems or between a system and a reservoir.

The basic principle underlying this phenomenon is the so-called ''thermoacoustic'' effect which generally refers to interaction between sound and heat. Investigations of this effect date back to the original work of Rayleigh [1], who analyzed pressure oscillations induced by a heat source in a tube [2–4]. The reverse mechanism, namely the generation of temperature gradients by sound waves, has also been studied [5–10]. Recently, the latter applications have attracted renewed attention, because thermoacoustic refrigerators eliminate the need for potential harmful refrigerants such as CFCs. Another advantage of these devices is the very small number of moving parts required, potentially making them highly reliable.

Unfortunately, thermoacoustic refrigerators often suffer from poor efficiency. Means to overcome this limitation is the subject of several ongoing efforts which, in particular, target more sophisticated stack and/or enclosure designs (e.g., [11–12]). However, these efforts are faced with several difficulties, due to lack of fundamental knowledge regarding the flow structure in the neighborhood of the stack and the essential features of flow-acoustics interactions.

The analysis of thermoacoustic devices has in large part relied on quasi-1D approximations. In particular, interactions between the acoustic wave and the stack are typically studied using the Stokes solution for an oscillating stream over a plate, or analytical solution of oscillating 1D flow within a slot [6, 13]. The resulting predictions have been extensively tested against experimental data (e.g., [5, 8]). Briefly, very good agreement between quasi-1D theory and experiment is obtained when the ''drive ratio,'' defined as the ratio of acoustic pressure amplitude to mean pressure, is small. When the drive ratio is large, however, significant deviations between quasi-1D predictions and experimental data occur [8]. Potential causes behind the discrepancies are many; these include multi-dimensional effects, nonlinear acoustic waves and shocks, transition to turbulence, nonlinear flow-acoustics interactions, convective heat transfer, and heat losses.

This paper is part of an effort which aims at a fundamental study of the above phenomena. Here, we focus exclusively on multidimensional flow effects. Specifically, the objectives of the present effort are: (a) development of 2D physical and computational models for the simulation of the flow in the neighborhood of an idealized thermoacoustic stack and (b) application of these models to investigate fundamentals of unsteady flow within the device.

The adopted approach is based on a simplified, yet flexible, physical formulation which enables us to isolate the essential features of the flow. Since in most applications

0021-9991/96 $18.00

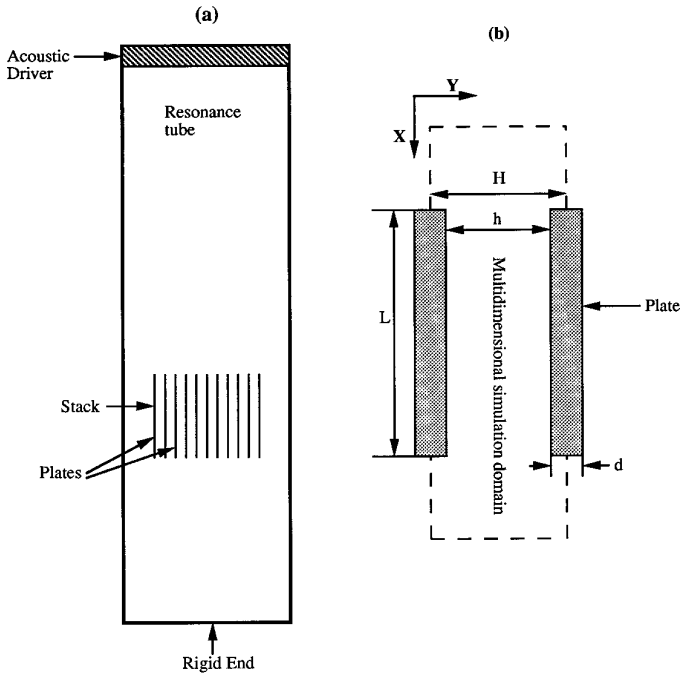

FIG. 1. Schematic illustration of a thermoacoustic refrigerator.

the acoustic wavelength is much larger than length of the thermoacoustic stack, it is neither realistic nor desirable to tackle the problem using a straightforward discretization approach. It is also obvious that since Mach numbers are typically small, a brute force multidimensional compressible flow simulation of the entire refrigerator should be avoided.

In order to tackle the scale complexity of the problem, we rely on the low Mach-number approximation of the governing equations to obtain a simplified model for the flow in a small neighborhood of the thermoacoustic stack. As discussed in section 2, the model represents the acoustic standing wave of unsteady boundary conditions on the computational domain. Within the domain, acoustic wave propagation is ignored, but leading order compressibility effects are retained in terms of spatially uniform thermodynamic variations. Flowfield simulation is based on numerical integration of the vorticity form of the governing equations. As discussed in Section 3, second-order centered differences are used to discretize the resulting system, and two variants of the technique are developed for the solution of discrete elliptic operators. The first is a standard Gaussian elimination solver; the second combines domain decomposition, boundary Green's function, and fast Poisson solution techniques. In Section 4, the model is applied to analyze the unsteady flow around a thermoacoustic stack operating at low drive ratio. Computations are used to examine vorticity dynamics and energy losses for a large matrix of operating conditions and stack configurations. Major conclusions are summarized in Section 5.

2. FORMULATION

The formulation of the physical model is based on four major assumptions: (a) the size of the thermoacoustic stack is much smaller than that of the resonance tube; (b) acoustic pressure amplitudes are small with respect to the mean, i.e., the Mach number is small; (c) far from the stack, the flow field is well approximated by an ideal acoustic standing wave; and (d) the medium within the device obeys the perfect gas law, is Newtonian, and has constant viscosity and thermal conductivity. Thus, the low Mach-number limit of the conservation equations provides an appropriate description of the flow in a small neighborhood of the stack; it is therefore adopted.

The above assumptions enable us to follow a construction which is similar to that used in a large number of reacting flow models, e.g., [14–17]. We start from the governing equations for compressible nonreacting ideal gas flow, normalized with respect to an appropriate combination of characteristic length, velocity, density, and pressure scales. The system of governing equations is expressed in terms of the mass, momentum, and energy conservation equations,

$$\frac{D\rho}{Dt} + \rho\nabla\cdot\mathbf{u} = 0 \tag{2.1}$$

$$\gamma M^2\rho\frac{D\mathbf{u}}{Dt} = -\nabla p + \frac{\gamma M^2}{\mathrm{Re}}\nabla\cdot\tau \tag{2.2}$$

$$\rho\frac{DT}{Dt} - \frac{\gamma-1}{\gamma}\frac{Dp}{Dt} = -\frac{1}{\mathrm{Pe}}\nabla\cdot\mathbf{q} + \frac{(\gamma-1)M^2}{\mathrm{Re}}\Theta, \tag{2.3}$$

together with the equation of state:

$$p = \rho T. \tag{2.4}$$

Here, $\mathbf{u}$ is the velocity vector, ρ is the density, $D/Dt = \partial/\partial t + \mathbf{u}\cdot\nabla$ is the material derivative, p is pressure, τ is the shear stress tensor, T is temperature, $\mathbf{q}$ is the heat flux vector, Θ is the viscous dissipation function, and γ is the specific heat ratio. Note that Eqs. (2.1)–(2.4) contain three dimensionless groups: the Reynolds number, Re, the Peclet number, Pe $\equiv$ RePr, where Pr is the Prandtl number; and, the Mach number M (see Section 2.1).

Next, we expand all relevant gasdynamic quantities in terms of powers of $\varepsilon \equiv \gamma M^2$, where γ is the specific heat ratio and M is the Mach number. Thus, a generic gasdynamic variable $\zeta(\mathbf{x}, t)$ is expressed in series form,

$$\zeta(\mathbf{x}, t) = \zeta_0(\mathbf{x}, t) + \varepsilon\zeta_1(\mathbf{x}, t) + \varepsilon^2\zeta_2(\mathbf{x}, t) + \cdots. \tag{2.5}$$

Substituting the appropriate expansions into the momentum equations and collecting the zeroth power in ε immediately yields

$$\nabla p_0 = 0; \tag{2.6}$$

i.e., the zeroth component of pressure is spatially uniform and, therefore, a function of time only. We shall refer to p_0 as the "thermodynamic" pressure and denote it by $P(t)$. To first order in ε, the momentum equation reads

$$\rho_0 \frac{D\mathbf{u}_0}{Dt} = -\nabla p_1 + \frac{1}{\mathrm{Re}} \nabla \cdot \tau. \tag{2.7}$$

Meanwhile, the leading-order energy equation for a fluid with constant thermal conductivity is given by

$$\rho_0 \frac{DT_0}{Dt} - \frac{\gamma - 1}{\gamma} \frac{dP}{dt} = \frac{1}{\mathrm{Pe}} \nabla^2 T. \tag{2.8}$$

Note that the energy balance is independent of p_1 and that viscous dissipation has been neglected.

A more convenient form of the energy equation is obtained by differentiating the leading order equation of state and by combining with the continuity equation to get

$$\nabla \cdot \mathbf{u}_0 = -\frac{1}{\gamma P} \frac{dP}{dt} + \frac{1}{P} \frac{1}{\mathrm{Pe}} \nabla^2 T. \tag{2.9}$$

Note that integration of Eq. (2.9) over the entire domain yields

$$\frac{V}{\gamma} \frac{dP}{dt} = -P \int \mathbf{u}_0 \cdot \mathbf{n} \, dA + \frac{1}{\mathrm{Pe}} \int \nabla T \cdot \mathbf{n} \, dA. \tag{2.10}$$

Thus, the time evolution of the thermodynamic pressure is related to the net mass flux and heat transfer at the surfaces.

The low Mach-number approximation replaces the original system, Eqs. (2.1)–(2.3), with the leading-order system, Eqs. (2.7)–(2.9). However, to facilitate the numerical implementation, we seek the vorticity form of the equations of motion. To this end, we first decompose the velocity field into divergence-free and irrotational parts; i.e., we let

$$\mathbf{u}_0 = \nabla \phi + \nabla \times \psi, \tag{2.11}$$

where ϕ is the velocity potential and ψ is the streamfunction. Substituting Eq. (2.11) into Eq. (2.9), one gets

$$\nabla^2 \phi = \frac{1}{P} \left[-\frac{1}{\gamma} \frac{dP}{dt} + \frac{1}{\mathrm{Pe}} \nabla^2 T \right]. \tag{2.12}$$

Second, taking the curl of the momentum equation and using the fact that the fluid has constant viscosity, we obtain

$$\frac{\partial \omega}{\partial t} + \nabla \times (\omega \times \mathbf{u}) = -\frac{\nabla \rho_0}{\rho_0} \times \frac{D\mathbf{u}}{Dt} + \frac{1}{\rho_0 \mathrm{Re}} \nabla^2 \omega. \tag{2.13}$$

Derivation of Eq. (2.13) completes the construction of the physical model, whose vorticity form consists of Eqs. (2.4), (2.8), (2.11)–(2.13), and the familiar vorticity–streamfunction relationship, $\nabla^2 \psi = -\omega$. For clarity and convenience, the subscripts 0, 1 will be omitted in the presentation below.

2.1. Normalization

Despite the relative simplicity of the geometry of the thermoacoustic stack, there exists a multitude of appropriate conventions which can be adopted in the normalization of the governing equations. (For a lucid application of dimensional arguments to thermoaccoustic devices see [18]). Thus, it is worthwhile, providing a clear description of normalizing parameters and of the meaning of the resulting dimensionless groups. Below, we use tildes to denote dimensional quantities and adopt the convention that all reference properties of the gas are taken at the mean temperature and pressure. Furthermore, we choose the plate separation distance, $\tilde{H}$, as a reference lengthscale, and $\tilde{\Omega}^{-1}$, the inverse of the angular frequency of the acoustic wave, as a reference timescale. This choice naturally leads to the definition of the reference velocity scale $\tilde{\Omega}\tilde{H}$ and of the Reynolds number:

$$\mathrm{Re} \equiv \frac{\tilde{\Omega} \tilde{H}^2}{\tilde{\nu}}. \tag{2.14}$$

We shall also refer to Re as the "kinematic" or "Stokes layer" Reynolds number since it effectively relates the thickness of the Stokes layer [13],

$$\tilde{\delta} \approx 6.4 \sqrt{\tilde{\nu}/\tilde{\Omega}}, \tag{2.15}$$

to the plate spacing, $\tilde{H}$, through

$$\frac{\tilde{\delta}}{\tilde{H}} \approx \frac{6.4}{\sqrt{\mathrm{Re}}}. \tag{2.16}$$

Other useful conventions for the Reynolds number include the "acoustic amplitude Reynolds number,"

$$\mathrm{Re}_a \equiv \frac{2\tilde{a}}{\sqrt{\tilde{\nu}\tilde{\Omega}}} \tag{2.17}$$

which is a dynamic Reynolds number based on the acoustic wave velocity amplitude, $\tilde{a}$, the thickness of the Stokes

layer, and the kinematic viscosity. The significance of Re_a has been discussed by Merkli and Thomann [19] who experimentally analyzed the flow field in an ''unobstructed'' resonance tube. In particular, it is shown in [19] that Re_a can be used to determine whether the (Stokes) boundary layers are stable or undergo transition to turbulence. As discussed below, values of Re_a used in the present study are ''subcritical''; transition to turbulence is therefore not expected.

The kinematic and dynamic Reynolds numbers can be related to each other through the ''particle displacement parameter,''

$$R_p \equiv \frac{\tilde{a}}{\tilde{\Omega}\tilde{H}}, \tag{2.18}$$

where $\tilde{a}$ is the dimensional acoustic velocity amplitude that would prevail in an unobstructed tube at the relevant stack location. Note that R_p characterizes the ratio of a characteristic particle displacement during a wave cycle to the plate separation distance. Combining Eq. (2.14) with Eqs. (2.17)–(2.18) yields

$$\mathrm{Re}_a{}^2 = 4\,\mathrm{Re}\,R_p{}^2. \tag{2.19}$$

Following the above discussion, the operating conditions of a thermoacoustic stack are determined in terms of the following set of dimensionless parameters: (a) one kinematic dimensionless group, i.e., Re or R_p; (b) the dynamic Reynolds number, Re_a, or equivalently, the acoustic drive ratio, Dr; (c) either the Prandtl number, $\mathrm{Pr} \equiv \tilde{\nu}/\tilde{\alpha}$, or the Peclet number,

$$\mathrm{Pe} \equiv \tilde{\Omega}\tilde{H}^2/\tilde{\alpha}; \tag{2.20}$$

(d) a stack configuration parameter, e.g., the blockage ratio $\tilde{h}/\tilde{H}$; (e) A plate length parameter, e.g., the plate length to spacing ratio, $\tilde{L}/\tilde{H}$, or the plate aspect ratio, $\tilde{L}/\tilde{d}$ (Fig. 1); and (f) the location of the thermoacoustic stack with respect to the driving acoustic wave, e.g., in terms of a dimensionless wavenumber $\tilde{\kappa}\tilde{x}$ (see Section 4).

2.2. Adiabatic Flow Submodel

As shown in the previous section, flowfield dynamics in the neighborhood of the stack are described in terms of six dimensionless groups. In order to avoid numerical experimentation in a six-dimensional parameter space, and in order to focus on the essential features of the flow, we restrict our attention to systems operating at low drive ratio. In these situations, significant temperature differences are not expected to develop within the stack [8] and the effects of thermal stratification on the evolution of the flow may be ignored. In particular, baroclinic vorticity generation may be neglected, and the vorticity transport equation reduces to

$$\frac{\partial \omega}{\partial t} + \nabla \times (\omega \times \mathbf{u}) = \frac{1}{\rho\,\mathrm{Re}}\nabla^2\omega. \tag{2.21}$$

Note, however, that Eq. (2.21) differs from the vorticity transport equation for incompressible flow in two aspects: (i) the effect of flowfield divergence is still retained and (ii) the effective diffusion coefficient is a density-scaled Reynolds number.

Since we are primarily interested in the velocity field and since in the limit of small density differences the vorticity transport equation decouples from the energy equation, we may further assume that the gas and the plates are thermally nonconducting. When this latter simplification is implemented, the energy equation reduces to its infinite Peclet number limit,

$$\rho\frac{DT}{Dt} - \frac{\gamma - 1}{\gamma}\frac{dP}{dt} = 0, \tag{2.22}$$

which is easily recognized as the isentropic compression law. Accordingly, the temperature, pressure, and density fields may be approximated in terms of analytical expressions for the idealized acoustic wave. This approximation is consistent with our assumption that the size of the stack is much smaller than the acoustic wavelength, so that acoustically related gradients may be locally ignored.

Finally, we note that the above assumption also enables us to simplify representation of the acoustic standing wave. In the present simplified formulation, the latter may be modeled by imposing either pressure oscillations, density oscillations, temperature oscillations, or oscillating velocity boundary conditions. As indicated in the following section, we have selected the latter option, which proves most convenient in the present setting.

3. NUMERICAL SCHEMES

3.1. Time Integration

Two-dimensional simulations of the model equations are performed using a finite difference methodology. To this end, the computational domain is divided using a rectangular grid with mesh size $\Delta x = \Delta y$. All spatial derivatives are discretized using standard second-order centered differences, and all source terms are explicitly integrated using the third-order Adams–Bashforth scheme [20]. Thus, assuming that the velocity field is known at time level $t = n\Delta t$, time integration is summarized as follows: (a) Integrate the ''bulk continuity'' equation in order to determine the thermodynamic pressure at the new time step,

$$\frac{P^{n+1}-P^n}{\Delta t}=\frac{\gamma}{V}\sum_{j=0}^{2}\beta_j P^{n-j}\int \mathbf{u}^{n-j}\cdot\mathbf{n}\,dA, \tag{3.1}$$

with $\beta_0=\frac{23}{12}$, $\beta_1=-\frac{16}{12}$, and $\beta_2=\frac{5}{12}$. (b) Determine the new density value ρ^{n+1} using the isentropic compression law,

$$\rho^{n+1}=\rho^n\left(\frac{P^{n+1}}{P^n}\right)^{1/\gamma} \tag{3.2}$$

and the new temperature value, T^{n+1}, using the equation of state,

$$T^{n+1}=P^{n+1}/\rho^{n+1}. \tag{3.3}$$

(c) Integrate the vorticity transport equation in order to determine the new vorticity distribution in the interior of the computational domain,

$$\frac{\omega^{n+1}-\omega^n}{\Delta t}=\sum_{j=0}^{2}\beta_j \left[\nabla_h\times(\mathbf{u}^{n-j}\times\omega^{n-j})+\frac{1}{\rho^{n-j}\,\mathrm{Re}}\nabla_h^2\omega^{n-j}\right], \tag{3.4}$$

where ∇_h and ∇_h^2 respectively denote the centered difference approximations to the gradient and Laplacian operators,

$$\nabla_h f_{i,j}=\begin{Bmatrix}\dfrac{f_{i+1,j}-f_{i-1,j}}{2\Delta x}\\[2ex] \dfrac{f_{i,j+1}-f_{i,j-1}}{2\Delta y}\end{Bmatrix} \tag{3.5}$$

and

$$\nabla_h^2 f_{i,j}=\frac{f_{i+1,j}-2f_{i,j}+f_{i-1,j}}{\Delta x^2}+\frac{f_{i,j+1}-2f_{i,j}+f_{i,j-1}}{\Delta y^2}. \tag{3.6}$$

(d) Reconstruct the velocity field at the new time step based on the updated vorticity field.

Steps (a)–(d) are repeated successively to obtain a time resolved approximation of unsteady motion. Except for step (d) which is further discussed below, the scheme involves standard substitutions and algebraic manipulations. Discussion of these operations is therefore omitted.

3.2. Velocity Field

Reconstruction of the velocity field and determination of boundary vorticity values are the more delicate aspects of the numerical scheme. It is therefore worthwhile providing a summary of the relevant procedures. Recall that the velocity field is expressed as the sum of an irrotational velocity—given as the gradient of a velocity potential, ϕ—and a divergence-free velocity—expressed as the curl of the streamfunction, ψ. Since both ϕ and ψ obey Poisson's equation, appropriate boundary conditions must be imposed.

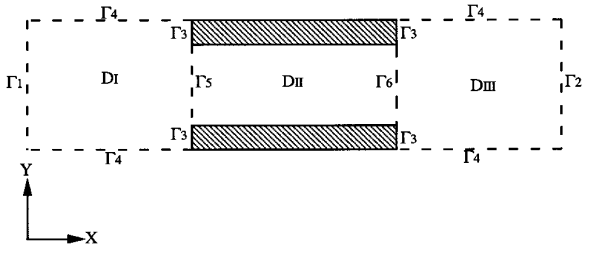

FIG. 2. Schematic illustration of the computational domain. For the domain decomposition technique, internal boundaries Γ_5 and Γ_6 are introduced, leading to the definition of three subdomains D_{I}, D_{II}, and D_{III}.

To this end, the boundary of the computational domain is divided into four subsets $\partial D=\Gamma_1\cup\Gamma_2\cup\Gamma_3\cup\Gamma_4$, as illustrated in Fig. 2. Γ_1 and Γ_2 are streamwise surfaces which limit the extent of the computational domain. They are referred to as "acoustic matching surfaces" (or simply matching surfaces), since the velocity field is assumed to match the idealized standing wave prediction at these locations. Γ_3 represents the skin of the plates, while Γ_4 is a periodicity boundary which models the presence of a large number of identical plates within the stack.

3.2.1. *Potential Distribution*

The velocity potential is specified so that it corresponds to the ideal flow that would exist within the channel in the case of an inviscid medium. Thus, it obeys the Poisson equation,

$$\nabla_h^2\phi^{n+1}=-\frac{1}{\gamma P^{n+1}}\frac{dP^{n+1}}{dt}, \tag{3.7}$$

with homogeneous Neumann conditions on Γ_3, periodicity conditions on Γ_4, and

$$\begin{aligned}\frac{\partial\phi^{n+1}}{\partial n}&=u_{a,1}(t^{n+1}),\quad \text{on }\Gamma_1,\\ \frac{\partial\phi^{n+1}}{\partial n}&=u_{a,2}(t^{n+1}),\quad \text{on }\Gamma_2,\end{aligned} \tag{3.8}$$

where $u_{a,1}(t)$ and $u_{a,2}(t)$ denote the acoustic velocities *imposed* on Γ_1 and Γ_2, respectively. Note that, due to the symmetry of the configuration, periodicity boundary conditions may be replaced by homogeneous Neumann condi-

tions. The solvability condition for the resulting Neumann problem is guaranteed by the bulk continuity equation,

$$\frac{V}{\gamma P^{n+1}}\frac{dP^{n+1}}{dt} = u_{a,1}(t^{n+1}) - u_{a,2}(t^{n+1}). \tag{3.9}$$

Finally, it is also advantageous to note that since the imposed acoustic velocities $u_{a,1}(t)$ and $u_{a,2}(t)$ are simply oscillating in time, the above Neumann problem also has an oscillating source term and boundary conditions. Thus, as long as one nontrivial solution is found, the remaining solutions can be obtained by simple scaling of the known solution. Consequently, one nonvanishing solution is determined in a preprocessing step and is input into the computation. Second-order, one-sided differences are used at the boundaries and the system of linear equations is inverted using a banded, unpivoted, Gaussian elimination routine. The latter is taken from the LINPACK library installed on the CRAY C90 at the Pittsburgh Supercomputer Center (PSC).

3.2.2. *Streamfunction Distribution*

Selection of boundary conditions for the streamfunction Poisson equation,

$$\nabla_h^2 \psi^{n+1} = -\omega^{n+1}, \tag{3.10}$$

is more involved than in the previous case, except perhaps for the obvious periodicity condition on Γ_4. A more detailed discussion is therefore provided.

Following the convention adopted in the previous section, the vorticity-induced velocity component is regarded as a nonlinear viscous perturbation to an otherwise ideal flow. Moreover, since the potential velocity component ''carries'' the entire volume flux through the domain, the stream function distribution may not induce any mean flow. Thus, it is appropriate to set a homogeneous Dirchlet boundary condition on solid surfaces, $\psi^{n+1} = 0$ on Γ_3.

Selection of streamfunction boundary conditions on matching surfaces is considerably more complicated, although various possibilities exist. Since we do not expect any significant vorticity migration from the plates towards the matching surfaces, any proper combination of homogeneous Drichlet or Neumann boundary conditions appears appropriate. The same is true for the vorticity on the matching surfaces. A Dirichlet-inflow/Neumann-outflow vorticity boundary condition appears to be well-suited there.

As indicated in Section 4.7, we have experimented with a large set of vorticity-streamfunction boundary conditions. For the time being, however, and unless otherwise noted, homogeneous Dirichlet boundary conditions on the matching surfaces are assumed, i.e., $\psi^{n+1} = 0$ on Γ_1 and Γ_2. Thus, the streamfunction obeys a Dirichlet/periodic Poisson problem, whose solution is further discussed in Section 3.2.3.

In conjunction with the above steamfunction boundary condition, the following approach is used to determine the boundary vorticity: (a) Vorticity values on periodicity surfaces, Γ_4, are found by direct integration of the vorticity transport equation. (b) ''Inflow/outflow'' boundary conditions are used on matching surfaces; we use

$$\begin{aligned} &\omega^{n+1} = 0, \quad \text{for } u_{a,1}(t^{n+1}) \geq 0, \\ &\frac{\partial \omega^{n+1}}{\partial x} = 0, \quad \text{otherwise}, \end{aligned} \tag{3.11}$$

on Γ_1, and

$$\begin{aligned} &\omega^{n+1} = 0, \quad \text{for } u_{a,2}(t^{n+1}) \leq 0, \\ &\frac{\partial \omega^{n+1}}{\partial x} = 0, \quad \text{otherwise}, \end{aligned} \tag{3.12}$$

on Γ_2. (c) On solid surfaces, vorticity boundary conditions are determined so that the no-slip condition is satisfied. Numerical boundary conditions are derived based on Taylor expansions of the vorticity–streamfunction relationship at a solid wall, and on (second-order) estimates of potential slip velocities at solid walls. Both first-order and second-order vorticity boundary conditions are adapted in different versions of the computations; for boundary point (j, k) on a wall with normal in the $-y$ direction, these are respectively expressed as [20]

$$\omega_{j,k} = \frac{2u_{s,k}}{\Delta y} + \frac{2}{\Delta y^2}(\psi_{j,k} - \psi_{j,k-1}) \tag{3.13}$$

and

$$\omega_{j,k} = \frac{3u_{s,k}}{\Delta y} - \frac{0.5}{\Delta y^2}(-7\psi_{j,k} + 8\psi_{j,k-1} - \psi_{j,k-2}), \tag{3.14}$$

where $u_{s,k}$ denotes the potential slip velocity at the boundary point. Discussion of both of these approximations is postponed until Section 4.7.

3.2.3. *Solutions of Streamfunction–Vorticity Equation*

Unlike the Neumann problem for the velocity potential which in the present adiabatic model is inverted only once, inversion of the streamfunction Poisson equation must be performed at every computational time step. Two different procedures were incorporated into different variants of the computations. The first is analogous to that described in Section 3.1. Specifically, in a preprocessing step, the system matrix is factored in a banded LU-form

using the relevant LINPACK library routines. Substitution is then performed at each time step.

Development of the second procedure is motivated primarily by a desire to reduce memory requirements and also to perform linear system inversion more rapidly. To this end, we first decompose the computational domain into three regions. As sketched in Fig. 2, the decomposition is performed by introducing two computational boundaries, Γ_5 and Γ_6, which coincide with the "streamwise" boundaries of the channel separating two neighboring plates.

Streamfunction distributions are then obtained by: (a) requiring that Eq. (3.10) holds at interior points within each subdomain, (b) retaining original boundary conditions, and (c) requiring continuity of the streamfunction and its normal derivatives at Γ_5 and Γ_6. Thus, the original problem is replaced by three elliptic systems which are coupled at the internal boundaries Γ_5 and Γ_6.

It appears at first that inversion of the corresponding systems must be simultaneously performed, at essentially the same cost as the original system. However, an attractive alternative is constructed by using a boundary Green's function technique to first decouple the three systems (e.g., [21]). Briefly, denoting by $\{\mathbf{z}_j\}_{j=1}^{M}$ the set of internal boundary points lying on Γ_5 and Γ_6, we first form the M elementary solutions,

$$\nabla_h^2 \tilde{\Psi}_j^\alpha = 0 \quad \text{in } D_\alpha, \tag{3.15}$$

where α = I, II, III, $j = 1, ..., M$ with boundary conditions on the internal boundaries:

$$\begin{aligned} &\tilde{\psi}_j^\alpha = 1, \quad \mathbf{x} = \mathbf{z}_j, \\ &\tilde{\psi}_j^\alpha = 0, \quad \text{otherwise.} \end{aligned} \tag{3.16}$$

Within each subdomain, the solution is expressed as a linear combination of the elementary solutions and the modified systems,

$$\nabla_h^2 \overline{\psi}^\alpha = -\omega^\alpha \quad \text{in } D_\alpha, \tag{3.17}$$

where α = I, II, and III with homogeneous Dirichlet boundary conditions at the internal boundaries. We thus write

$$\psi^\alpha = \overline{\psi}^\alpha + \sum_{j=1}^{M} \eta_j \tilde{\psi}_j^\alpha. \tag{3.18}$$

For arbitrary selection of the coefficient η_j, the corresponding streamfunction distribution given by Eq. (3.18) satisfies the governing equations except possibly for the normal-derivative boundary conditions on the streamfunction at the internal boundaries. (The latter are approximated using one-sided second-order differences within each of the corresponding subdomains). Requiring that these conditions be satisfied results in a linear system of equations for the η_j's. The inverse of the corresponding $M \times M$ influence matrix, denoted A^{-1}, is determined using Gaussian elimination in a preprocessing step, and then fed to the computations.

Thus, the inversion procedure for the streamfunction Poisson equation consists of four steps: (a) invert the three, decoupled, modified Poisson systems in Eq. (3.17); (b) select the right combination of elementary solutions using the inverse of the influence matrix; (c) determine the correct streamfunction distribution on the internal boundaries Γ_5 and Γ_6; and (d) solve the three decoupled systems with the correct boundary conditions substituted on Γ_5 and Γ_6.

The Green's function technique summarized above offers one additional advantage which is exploited in the computations. It is based on noting that the "system" matrices corresponding to Eq. (3.17) have a special structure. Specifically, they correspond to Poisson problems in rectangular domains, with either periodicity or homogeneous boundary conditions on opposing sides. Thus, the implementation of Fourier analysis techniques to further reduce storage and computational overheads proves particularly attractive.

Briefly, we use a discrete Fourier transform of the finite-difference equations in domains I and III to transform the original system and boundary conditions into a set of decoupled one-dimensional tri-diagonal systems for the Fourier coefficients. The latter are efficiently inverted using the Thomas algorithm [22, 23]. Determination of discrete Fourier coefficients and reconstruction of "physical" data are performed using the FFT routines of the ECMFFT package of the PSC C90 library.

A similar approach is adopted in domain II. The major difference is due to the fact that, since homogeneous Dirchlet streamfunction conditions are imposed at the channel boundaries, a discrete sine transform is used in lieu of discrete Fourier transforms. The remaining aspects of the numerical procedure are essentially identical to those we have just described.

Finally, it is emphasized that the discrete Fourier and sine function expansions used to accelerate the solution of the finite difference equations should not be identified with global spectral approximations of the numerical solutions. In fact, spectral approximations corresponding to the above expansions are *not* appropriate in the present setting. For instance, it is easy to verify that a sine function expansions within the channel naturally leads to a boundary vorticity distribution which vanishes identically. Thus, the expansions introduced above are only regarded as discrete transforms of discrete finite-difference "signals"; their implementation within this framework is obviously well justified.

TABLE I

Flow Conditions and Discretization Parameters

Case	Re	Re_a	h/H	L/H	$\tilde{k}\tilde{x}$	R_p	Dr	δ/H	$N_x^{\mathrm{l}} = N_x^{\mathrm{m}}$	$N_y^{\mathrm{l}} = N_y^{\mathrm{m}}$	$\Delta t \times 10^3$
1	2132	13.25	0.666	1.32	$\pi/2$	0.1435	0.2%	0.2	80	120	2.33
2	2132	33.15	0.666	1.32	$\pi/2$	0.358	0.5%	0.2	160	120	0.938
3	2132	66.27	0.666	1.32	$\pi/2$	0.717	1.0%	0.2	320	121	0.468
4	2132	9.53	0.666	1.32	$3\pi/4$	0.1031	0.2%	0.2	80	120	3.25
5	2132	23.8	0.666	1.32	$3\pi/4$	0.257	0.5%	0.2	160	120	1.30
6	2132	47.65	0.666	1.32	$3\pi/4$	0.515	1.0%	0.2	160	120	0.652
7	2132	13.25	0.583	1.32	$\pi/2$	0.1435	0.2%	0.2	80	120	2.30
8	2132	33.15	0.583	1.32	$\pi/2$	0.358	0.5%	0.2	160	120	0.938
9	2132	66.27	0.583	1.32	$\pi/2$	0.717	1.0%	0.2	320	121	0.468
10	2132	9.53	0.583	1.32	$3\pi/4$	0.1031	0.2%	0.2	80	120	3.25
11	2132	23.8	0.583	1.32	$3\pi/4$	0.257	0.5%	0.2	160	120	1.30
12	2132	47.64	0.583	1.32	$3\pi/4$	0.515	1.0%	0.2	320	121	0.652
13	2132	13.25	0.75	1.32	$\pi/2$	0.1435	0.2%	0.2	80	120	2.33
14	2132	33.15	0.75	1.32	$\pi/2$	0.358	0.5%	0.2	160	120	0.938
15	2132	66.27	0.75	1.32	$\pi/2$	0.717	1.0%	0.2	320	121	0.468
16	574	36	0.666	1.32	$\pi/2$	0.75	1.0%	0.4	320	121	0.448
17	256	20.83	0.666	1.32	$\pi/2$	0.65	1.0%	0.6	320	121	0.517
18	574	25.92	0.666	1.32	$3\pi/4$	0.54	1.0%	0.4	320	121	0.622
19	256	15.0	0.666	1.32	$3\pi/4$	0.469	1.0%	0.6	320	121	0.716
20	574	36	0.583	1.32	$\pi/2$	0.75	1.0%	0.4	320	121	0.448
21	256	20.83	0.583	1.32	$\pi/2$	0.65	1.0%	0.6	320	121	0.517
22	2132	66.27	0.666	4	$\pi/2$	0.717	1.0%	0.2	320	121	0.468
23	564	36	0.666	4	$\pi/2$	0.75	1.0%	0.4	320	121	0.448
24	256	20.83	0.666	4	$\pi/2$	0.65	1.0%	0.6	320	121	0.517
25	2132	66.27	0.666	6.66	$\pi/2$	0.717	1.0%	0.2	320	121	0.468
26	574	36	0.666	6.66	$\pi/2$	0.75	1.0%	0.2	320	121	0.448
27	256	20.83	0.666	6.66	$\pi/2$	0.65	1.0%	0.6	320	121	0.517

4. RESULTS AND DISCUSSION

Numerical schemes constructed above are applied to examine the fundamental features of the flow and their dependence on: (a) configuration parameters, namely the channel blockage ratio and plate aspect ratio; (b) flow parameters, specified using the acoustic and kinematic Reynolds numbers; and (c) the stack position, expressed in terms of a normalized wavenumber, $\tilde{k}\tilde{x}$. Here, $\tilde{k} \equiv 2\pi/\tilde{\lambda}$ is the dimensional wavenumber defined using the wavelength of the standing wave, $\tilde{\lambda}$, while $\tilde{x}$ is the physical distance along the tube measured from the rigid end (Fig. 1).

The selection of flow parameters is based on a desire to mimic conditions which are similar to those encountered in physical experiments and, at the same time, challenge the computations. Conditions similar to those in the experiments of Atchley *et al.* [8] are selected, since these are characterized by thin, well-separated Stokes layers. A large matrix of flow conditions is considered in the analysis, as summarized in Table I. Note that Table I describes the flow in terms of eight dimensionless parameters. Since a set of five parameters is sufficient to fully specify flow conditions in the current formulation (Section 2), Table I contains some redundancy. The latter is introduced intentionally, in order to facilitate discussion and interpretation of computed results. Table I also provides a summary of discretization parameters, which are also used to specify the location of matching surfaces with respect to the stack.

Construction of Table I is based on the following strategy. The stack configuration of cases 1–3 is taken as a reference configuration, and cases 1–3 are used to study the effects of the drive ratio. The analysis is repeated at $\tilde{k}\tilde{x} = 3\pi/4$ (cases 4–6), where the thermoacoustic coupling efficiency is expected to peak. The effect of blockage ratio h/H is examined in cases 7–15. Cases 7–9 and cases 13–15 correspond to the same flow conditions and stack position as in cases 1–3, but with different blockage ratios; $h/H = 0.583$ for cases 7–9, while $h/H = 0.75$ for cases 13–15. Similarly, cases 10–12 correspond to the same flow conditions as cases 4–6 but with smaller blockage ratio $h/H = 0.583$. The effect of boundary layer thickness to

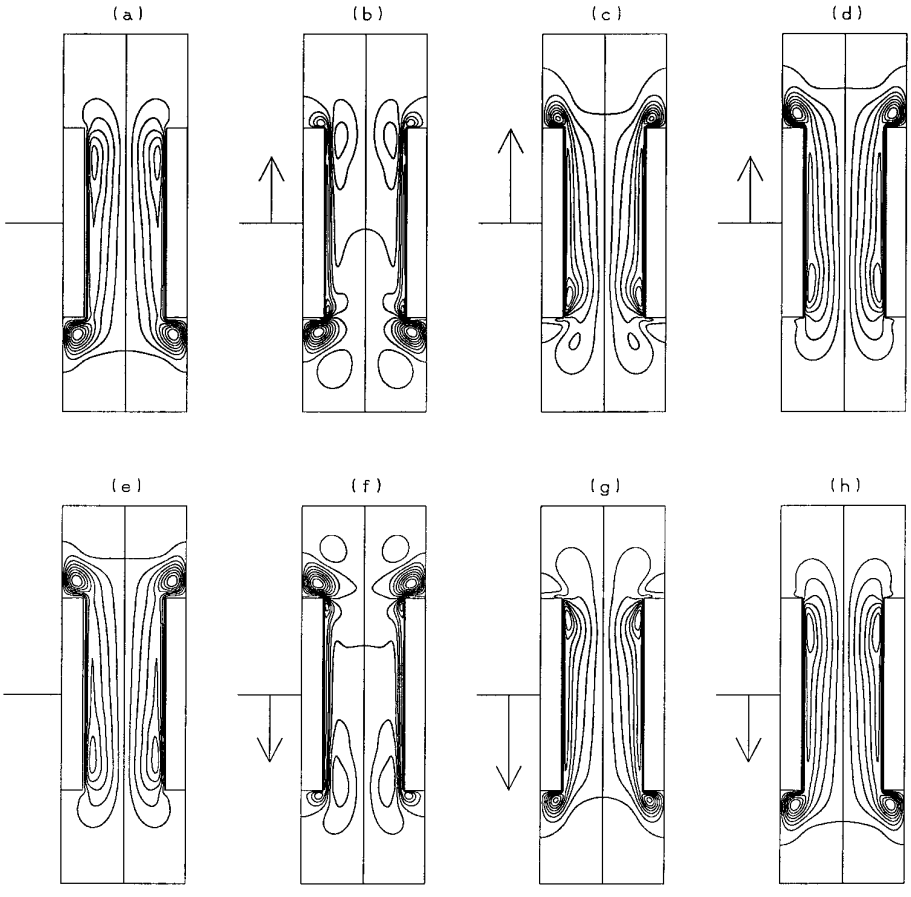

FIG. 3. Evolution of the streamfunction distribution for case 1. Contour plots are generated at (a) $t = 32\pi/4$, (b) $t = 33\pi/4$, (c) $t = 34\pi/4$, (d) $t = 35\pi/4$, (e) $t = 36\pi/4$, (f) $t = 37\pi/4$, (g) $t = 38\pi/4$, and (h) $t = 39\pi/4$.

plate separation ratio δ/H is studied by varying Re while keeping R_p essentially constant. In cases 16–17, the stack of case 3 is driven at $\delta/H = 0.4$ and 0.6, respectively. For the same δ/H ratios, different stack positions are considered in cases 18–19, while different blockage ratios are considered in cases 20–21. Finally, the effect of plate aspect ratio is analyzed by considering two additional plate length parameters, $L/H = 4$ and 6.66. Cases 22–24 are respectively ''derived'' from cases 3, 16, and 17 by increasing the plate length to $L/H = 4$. Meanwhile, cases 25–27 correspond to the same flow conditions as in cases 22–24, respectively, but for different plate aspect ratio, $L/H = 6.66$.

4.1. Essential Flow Features

Streamfunction distributions for cases 1–3, generated at $\frac{1}{8}$ cycle time intervals, are plotted in Figs. 3–5 respectively. In all cases, the computations are carried for five acoustic cycles in order to approach a ''stationary'' flow regime; the first four cycles are omitted from the analysis.

Evolution of the streamfunction distribution during an acoustic cycle is summarized as follows. Figure 3a is generated at the end of the fourth cycle, the time at which the acoustic velocities vanish at both matching surfaces. At this stage, the streamfunction distribution within the channel is essentially uniform, except for the ''top'' end of the stack, where a deformation reminiscent of a separation bubble may be observed. At the other end of the stack, the streamfunction contours show the presence of a pair of concentrated eddies located close to the plates and a weaker pair of vortices located close to the matching surface. As the flow accelerates upwards (Fig. 3b), the vortical structures located near the lower matching surface are pushed towards the edges of the plates and are deformed in the cross-stream direction. At the ''entrance of the channel,'' the streamfunction distribution suggests that a separation zone forms; a similar process can be observed at the channel ''exit.'' When the acoustic velocity magnitude reaches its first peak, Fig. 3c suggests that the vortical structures which existed ''upstream'' of the channel have almost been destroyed due to impingement at the plate edges. Meanwhile, the separation bubbles at the entrance and exit of the channel continue to intensify. This process continues even as the flow starts decelerating (Fig. 3d).

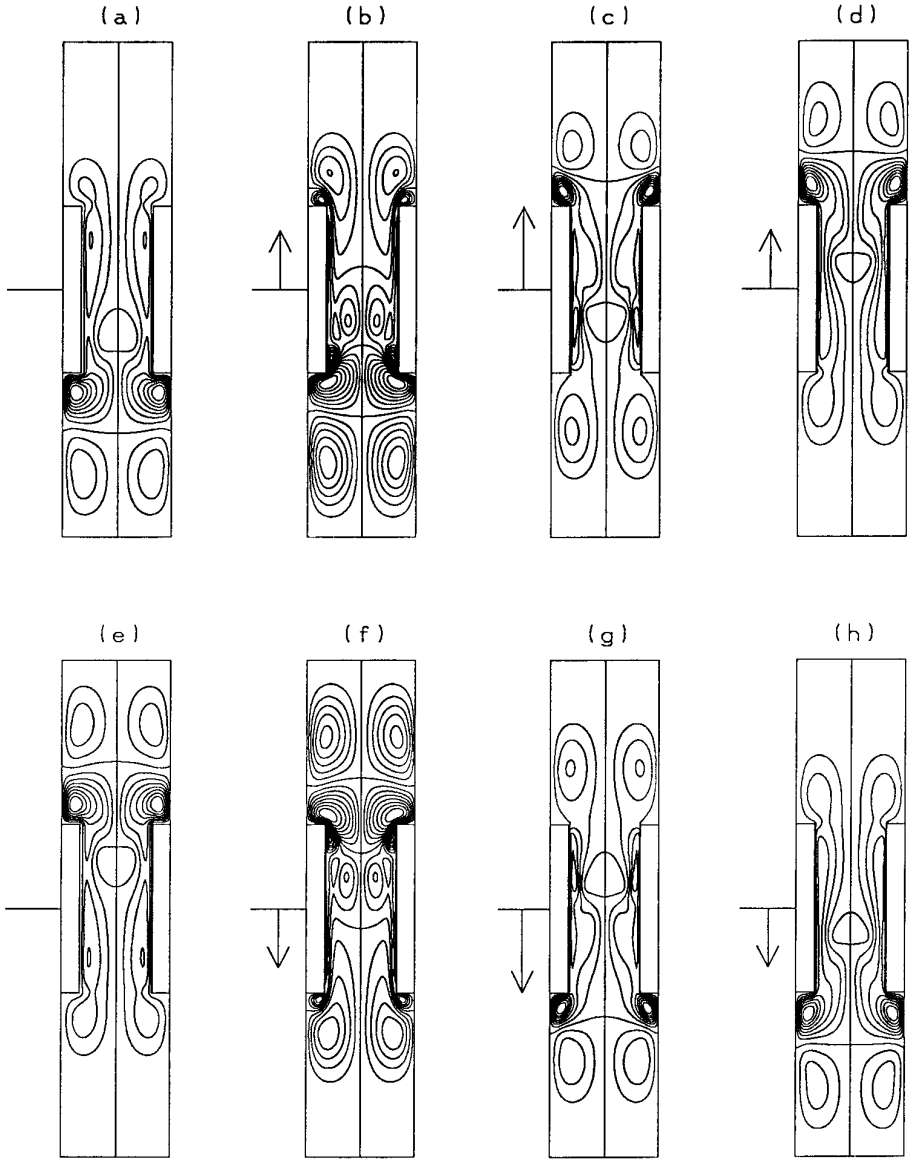

FIG. 4. Evolution of the streamfunction distribution for case 2. Contour plots are generated at (a) $t = 32\pi/4$, (b) $t = 33\pi/4$, (c) $t = 34\pi/4$, (d) $t = 35\pi/4$, (e) $t = 36\pi/4$, (f) $t = 37\pi/4$, (g) $t = 38\pi/4$, and (h) $t = 39\pi/4$.

Figures 3a and 3e are separated by one-half cycle; each is generated at a time when the acoustic velocity vanishes. The corresponding acoustic accelerations peak, but have opposite directions. Comparison of Figs. 3a and 3e shows that the streamfunction distribution at these two stages appear to be mirror images with respect to the horizontal mid-plane. This symmetry suggests that the process described above is reversed every half cycle. That this is in fact the case can be verified by comparing Figs. 3g–h with frames generated half a cycle earlier.

Figures 4 and 5 show that, while the essential features of flow acceleration and deceleration are similar to those described above, significant differences arise as the acoustic velocity amplitude is increased. In particular, the impingement of vortical structures on the faces of the stack plates at low drive ratio, $Dr = 0.2\%$, is dramatically different from that occurring at higher drive ratios, $Dr = 0.5\%$ and 1%. In the latter cases, the impingement of the vortices on the edges of the plates is better described by a breakup phenomenon, during which a portion of the eddy is destroyed and another portion rolls over the plate corners and penetrates the channel. The two vortices emanating from opposing plate edges migrate towards the channel centerline and stick together to form a vortex bubble,

which is advected in the channel under the influence of the mean flow.

The dynamics of this vortex bubble appear to depend on the drive ratio, or more precisely, the particle displacement parameter. Specifically, the vortex bubble always remains "trapped" in the channel for case 2. When the acoustic velocity amplitude increases (case 3), the same structure migrates to the end of the channel and is later ejected into the unobstructured region. Thus, when the particle displacement parameter is large, the vortex bubble is more likely to be ejected from the obstruction (within half a cycle or less) than is the case at low displacement parameter.

One of the advantages of the present implementation of the Helmholtz decomposition is that the streamfunction distribution does not carry any mean flow velocity. Thus, streamfunction contours may be directly used to characterize the vorticity distribution. However, one minor drawback is that the disparity between vorticity values in different cases prevents us from uniformly selecting increments in the streamfunction contours. Thus, these contours some-

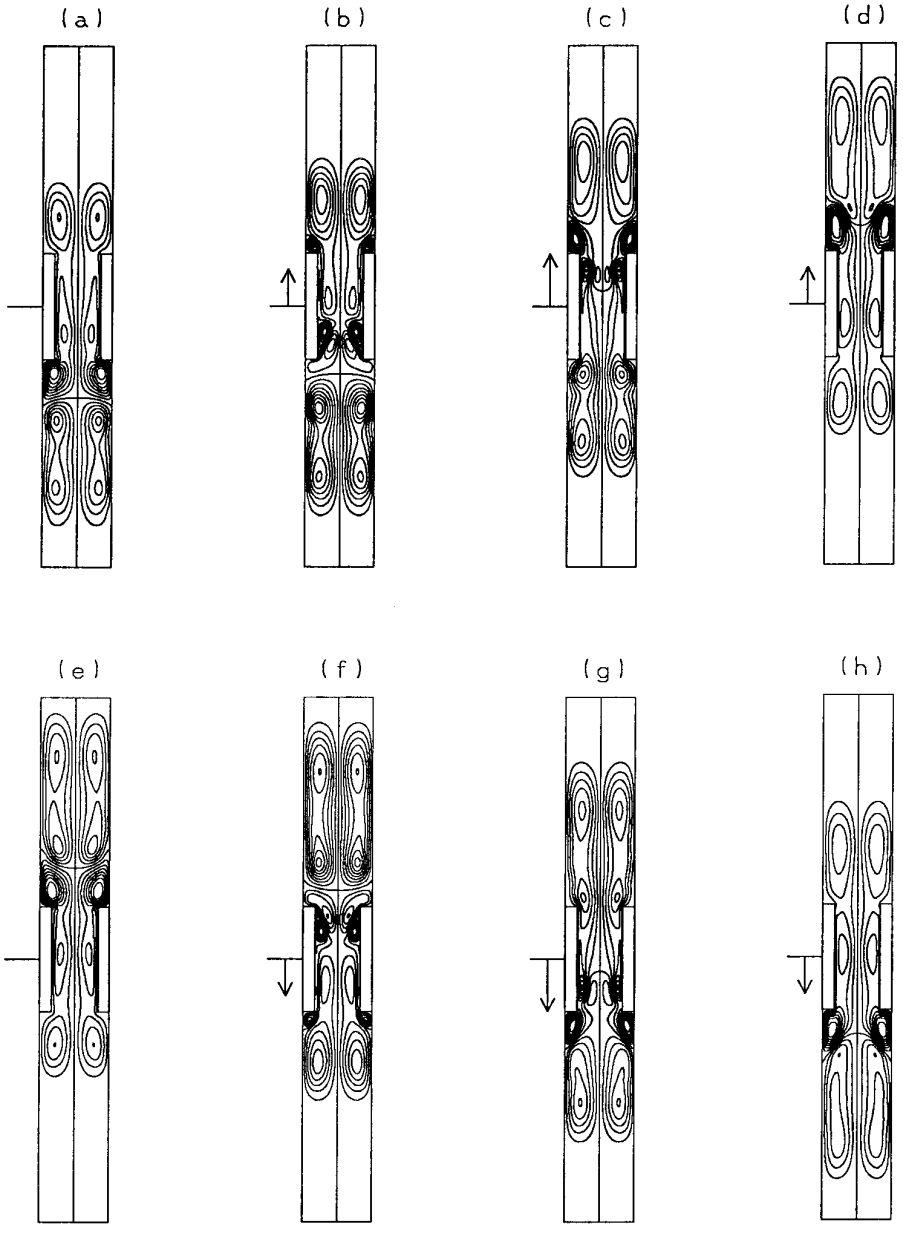

FIG. 5. Evolution of the streamfunction distribution for case 3. Contour plots are generated at (a) $t = 32\pi/4$, (b) $t = 33\pi/4$, (c) $t = 34\pi/4$, (d) $t = 35\pi/4$, (e) $t = 36\pi/4$, (f) $t = 37\pi/4$, (g) $t = 38\pi/4$, and (h) $t = 39\pi/4$.

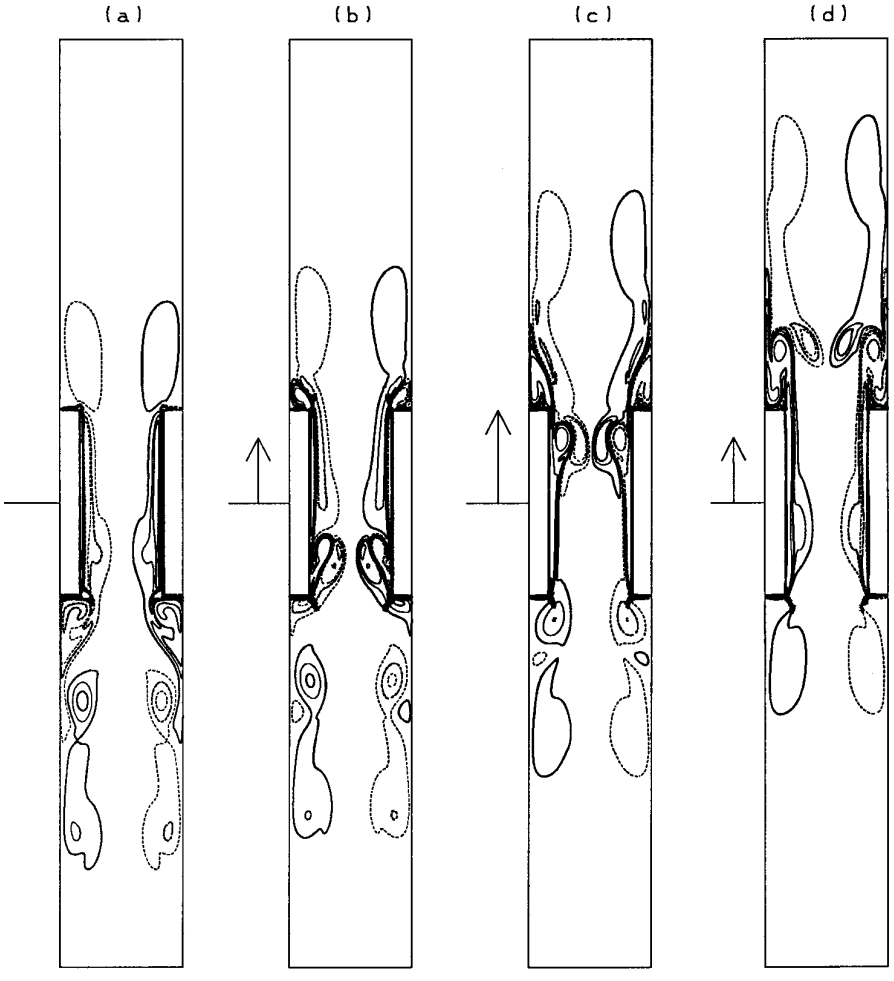

FIG. 6. Evolution of the vorticity field for case 3. Contour plots are generated at (a) $t = 32\pi/4$, (b) $t = 33\pi/4$, (c) $t = 34\pi/4$, and (d) $t = 35\pi/4$.

what hide the strength of vortical structures. A more serious disadvantage is that opposite signs of vorticity cannot be easily distinguished. To overcome this difficulty, we provide one set of vorticity contours and later rely on our experience in an abbreviated discussion of other cases.

Vorticity contours for the flow conditions of case 3 are plotted in Fig. 6. Following the above discussion only one half cycle is illustrated; thus, only four frames, generated at $\frac{1}{8}$ cycle time intervals, are provided. Figure 6 shows that near the channel plates the vorticity distribution is arranged in layers of opposite sign. This observation is in agreement with the prediction of the quasi-1D theory which leads us to expect Stokes layers at these locations. Since the vorticity of Stokes layers decays rapidly from the boundary, two primary layers can be clearly distinguished. Further analysis of computed data reveals that the vorticity can be closely approximated by a strong layer adjacent to the boundary, and a weaker one next to the first.

Figure 6 also shows that as the Stokes layer is shed from the plate edges, rollup of the corresponding vorticity field occurs in a peculiar fashion. The strong layer of vorticity is entrained along the sides of the plates and rolls to form a strong concentrated eddy. Meanwhile, the weaker vorticity layer appears to slide over the stronger layer and rolls to form a more elongated vortex structure. Thus, the shedding of the Stokes layer results in the formation of a pair of counterrotating vortices.

It is also interesting to note that the vorticity distribution is ''antisymmetric'' with respect to the channel centerline. An immediate consequence of this observation is that the vortex bubble seen in the streamfunction contours is in fact formed by the merger of two vortices of opposite signs. The formation of this bubble can also be observed in the vorticity contours, which indicate that the motion of the bubble along the channel centerline is accompanied by a depression in the Stokes layer ahead of the bubble. Behind the bubble, the opposite holds; i.e., the boundary layer appears to thicken as it is pulled away from the plate surface.

The antisymmetry of the vorticity field with respect to

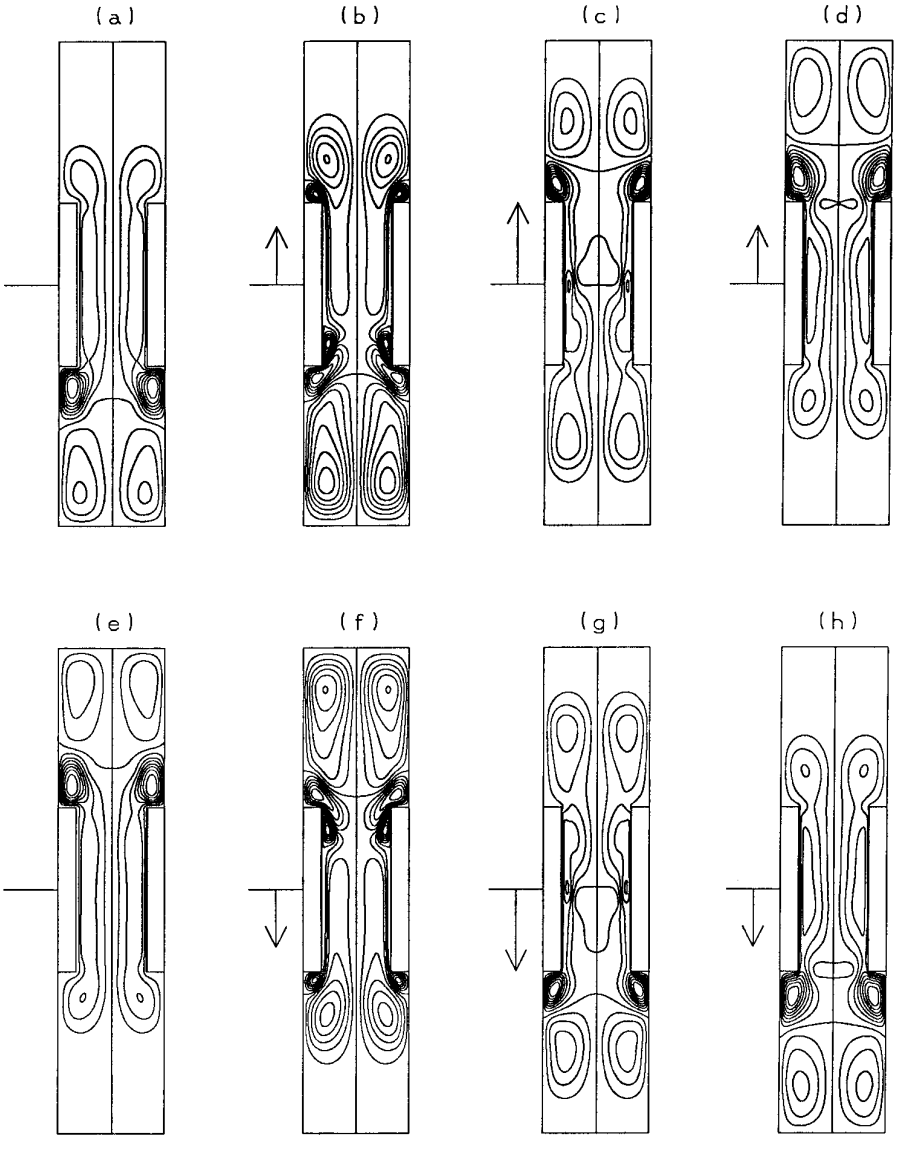

FIG. 7. Evolution of the streamfunction distribution for case 6. Contour plots are generated at (a) $t = 32\pi/4$, (b) $t = 33\pi/4$, (c) $t = 34\pi/4$, (d) $t = 35\pi/4$, (e) $t = 36\pi/4$, (f) $t = 37\pi/4$, (g) $t = 38\pi/4$, and (h) $t = 39\pi/4$.

the channel centerline is observed in all cases considered. Below, we exploit this feature in order to keep the presentation brief; details regarding the origin and formation of vortical structures will not be repeated. In addition, differences between various configurations and flow conditions are discussed using streamfunction distributions only.

4.2. Effect of Stack Position

As indicated earlier, the above analysis is repeated at $\tilde{k}\tilde{x} = 3\pi/4$. Here, we restrict our attention to case 6, for which streamfunction contours are plotted in Fig. 7. Comparison of Fig. 7 with Fig. 5 reveals that the streamfunction distributions for $\tilde{k}\tilde{x} = 3\pi/4$ and $\tilde{k}\tilde{x} = \pi/2$ have many features in common. In particular, the shedding of Stokes layers and the formation of counterrotating vortices occur in a similar fashion. Also similar are the broad features of vortex impingement on the sides of the plates and the subsequent generation of a vortex bubble within the obstructed region. However, the streamfunction distributions of Figs. 5 and 7 reveal one obvious difference. For $\tilde{k}\tilde{x} = 3\pi/4$ streamfunction plots generated one half cycle apart are no longer symmetric with respect to the horizontal mid-plane. In addition, differences are also detected in the

shedding of Stokes layers from different ends of the plates, and in the vortex structures which form following the shedding process. The phenomenon should be expected, since for stack located at $\tilde{k}\tilde{x} = 3\pi/4$, flowfield divergence does not vanish and acoustic velocities are different on different sides of the channel. Thus, in addition to flow unsteadiness, spatial acceleration of the medium also occurs due to finite divergence. For the present case, flowfield divergence occurs in such a way that the mean volume flux decreases in magnitude as one moves from the bottom matching surface towards the top.

The lack of symmetry with respect to the horizontal midplane is further examined in Fig. 8, where vorticity contours for case 6 are generated. Figure 8 indicates that the nonuniform flow acceleration and asymmetric shedding result in the formation of vortex structures of different shapes and strengths. In particular, it appears that vortices shed at the lower tube end are slightly stronger than those generated at the top.

Comparison of cases 3 and 6 shows a qualitative similarity in the structure of the vorticity field. However, more detailed examination of the results (not shown) reveals that vorticity concentrations are weaker for a stack located at $\tilde{k}\tilde{x} = 3\pi/4$ than at $\tilde{k}\tilde{x} = \pi/2$. This effect is expected, since local particle velocities are appreciably smaller at $\tilde{k}\tilde{x} = 3\pi/4$ than at the velocity antinode, $\tilde{k}\tilde{x} = \pi/2$.

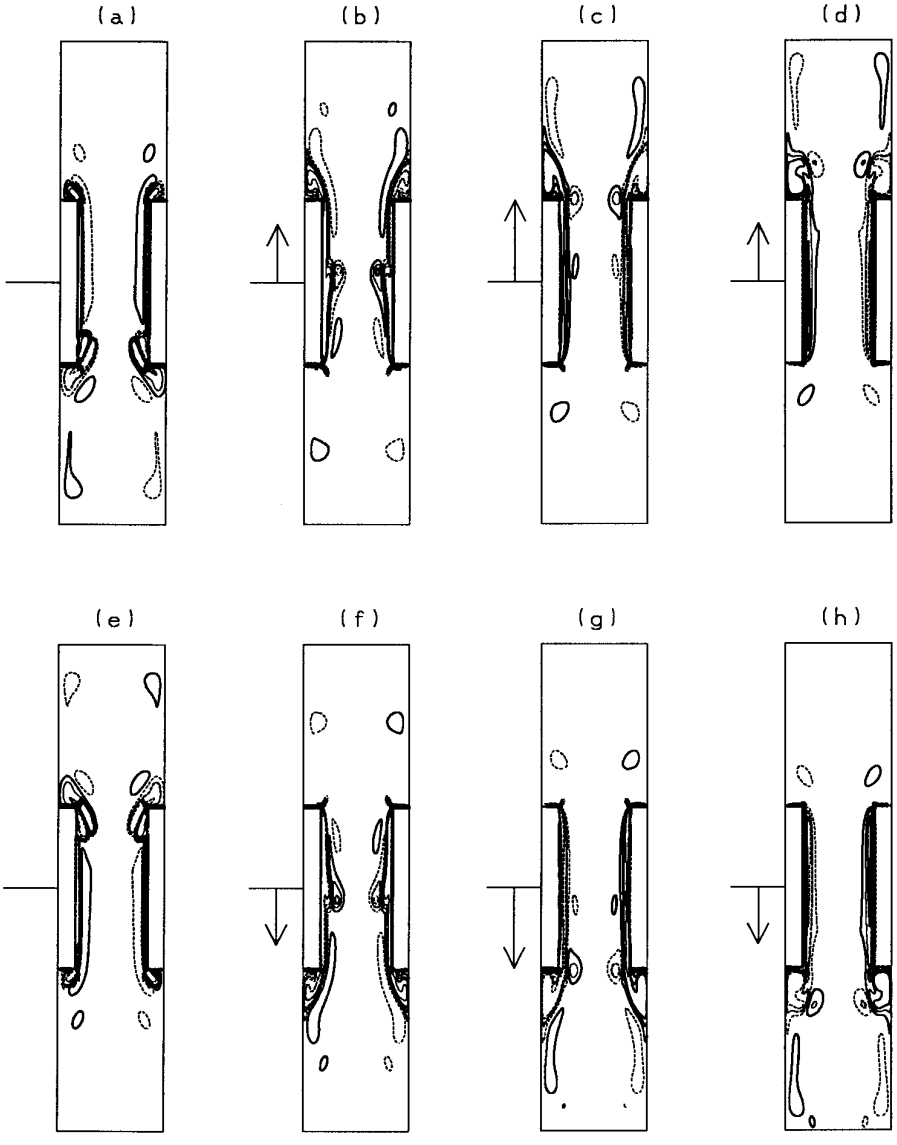

FIG. 8. Evolution of the vorticity field for case 6. Contour plots are generated at (a) $t = 32\pi/4$, (b) $t = 33\pi/4$, (c) $t = 34\pi/4$, (d) $t = 35\pi/4$, (e) $t = 36\pi/4$, (f) $t = 37\pi/4$, (g) $t = 38\pi/4$, and (h) $t = 39\pi/4$.

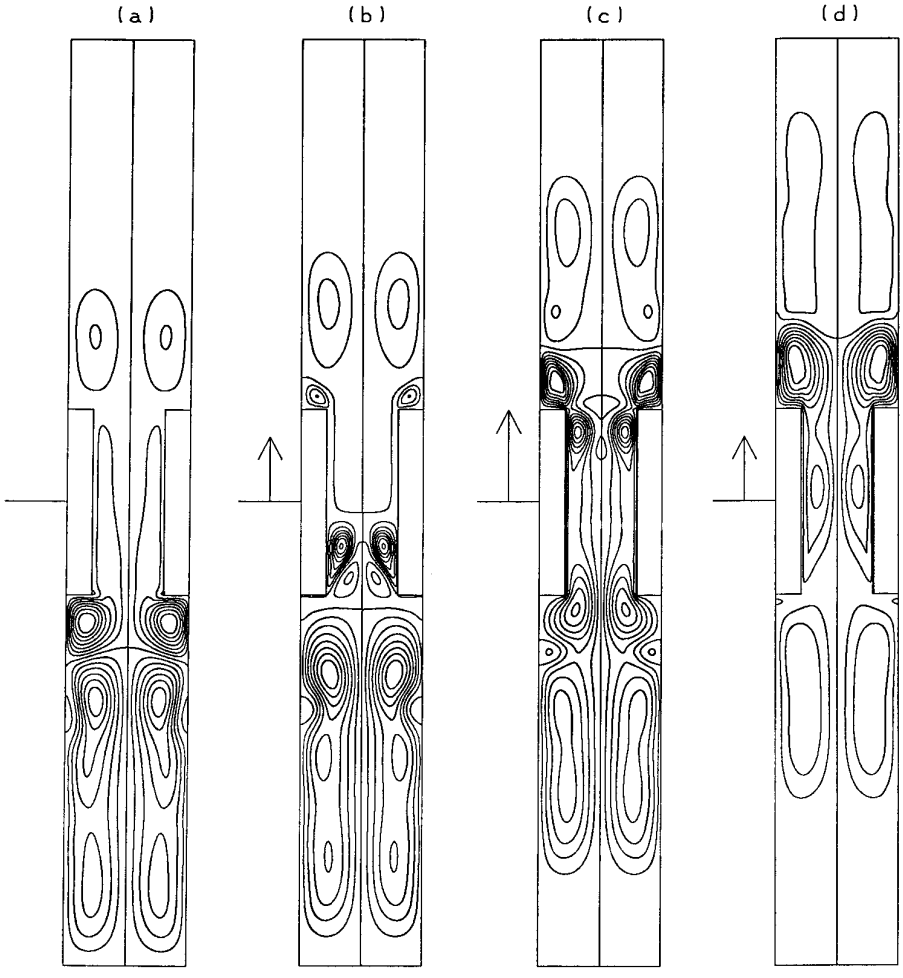

FIG. 9. Evolution of the streamfunction distribution for case 9. Contour plots are generated at (a) $t = 32\pi/4$, (b) $t = 33\pi/4$, (c) $t = 34\pi/4$, and (d) $t = 35\pi/4$.

4.3. Effect of Blockage Ratio

Discussion of the effects of blockage ratio is restricted to cases 9 and 15, i.e., to stacks located at a velocity node and driven at $Dr = 1\%$. While stacks located at $\tilde{k}\tilde{x} = 3\pi/4$ were also included in the analysis, as were different drive ratios, differences due to stack position and acoustic velocity amplitude followed the same trends established in the two subsections above; the corresponding results are therefore omitted.

Streamfunction distributions for cases 9 and 15 are plotted in Figs. 9 and 10, respectively. Simultaneous examination of Figs. 5, 9, and 10 reveals that modifying the blockage ratio, as presently implemented by altering the thickness of the plates, results in significant modulation of the flowfield. Several differences between cases 3, 9, and 15, respectively characterized by $h/H = 0.666$, 0.583, and 0.75 are observed. These differences, which primarily concern the shape of vortical structures and recirculation regions, and their impact on the global flow structure, are summarized as follows:

(a) The broad features of the flow for $h/H = 0.666$ and 0.75 are similar. However, for $h/H = 0.75$, the recirculation regions forming near the corners of the plates are obviously smaller. Not surprisingly, the impingement of these vortical structures on the sides of the plates leads to the formation of weaker vortex bubbles within the channel. Furthermore, the recirculation regions which form within the channel are less inclined with respect to the primary flow direction for $h/H = 0.75$ than is the case for $h/H = 0.666$. A global manifestation of these mechanisms is that, as the blockage ratio increases, smaller amounts of vorticity migrate towards the channel centerline. This observation can be verified by comparing streamline deformations near the channel centerline, as depicted in Figs. 5 and 10.

(b) More substantial differences can be detected as h/H is decreased to 0.583. One obvious and predictable

effect is that the size of recirculation regions located on the sides of the plates also increases. However, one notable difference is that the impingement of these vortices on the plate edges now leads to a more pronounced flow deformation. Specifically, the recirculation regions forming within the channel (''downstream'' of the vortex impingement) are much larger than those previously observed and are substantially more inclined with respect to the flow. Two opposing recirculation zones extend at a steep angle and touch at the channel centerline. Furthermore, these large recirculation zones appear to have sufficient strength to tear vorticity from the free counterrotating vortex pair located in the unobstructed region. This leads to the formation of multiple vortex bubbles within the channel, whose entire cross-section is ''polluted'' with strong patches of vorticity.

The dynamical behavior of the recirculation zones lying on the sides of plates is also affected by increasing the plate thickness. In particular, the organization of vorticity within these zones shows the presence of multiple vortex structures. We have not fully investigated the origin of this phenomenon, which may either be caused by the breakdown of the recirculation zone or, due to its interaction with boundary layers, on the plate sides.

4.4. Effect of Stokes Layer Thickness

The impact of boundary layer thickness is analyzed by contrasting results for cases 16 and 17 with predictions for case 3. Streamfunction distributions for cases 16 and 17 are plotted in Figs. 11 and 12, respectively.

Recall that cases 16 and 17 differ from case 3 in that Re is altered in such a way that δ/H increases from 0.2 (case 3) to 0.4. (case 16) and 0.6 (case 17). In doing so, we have attempted to avoid significantly changing the prevailing

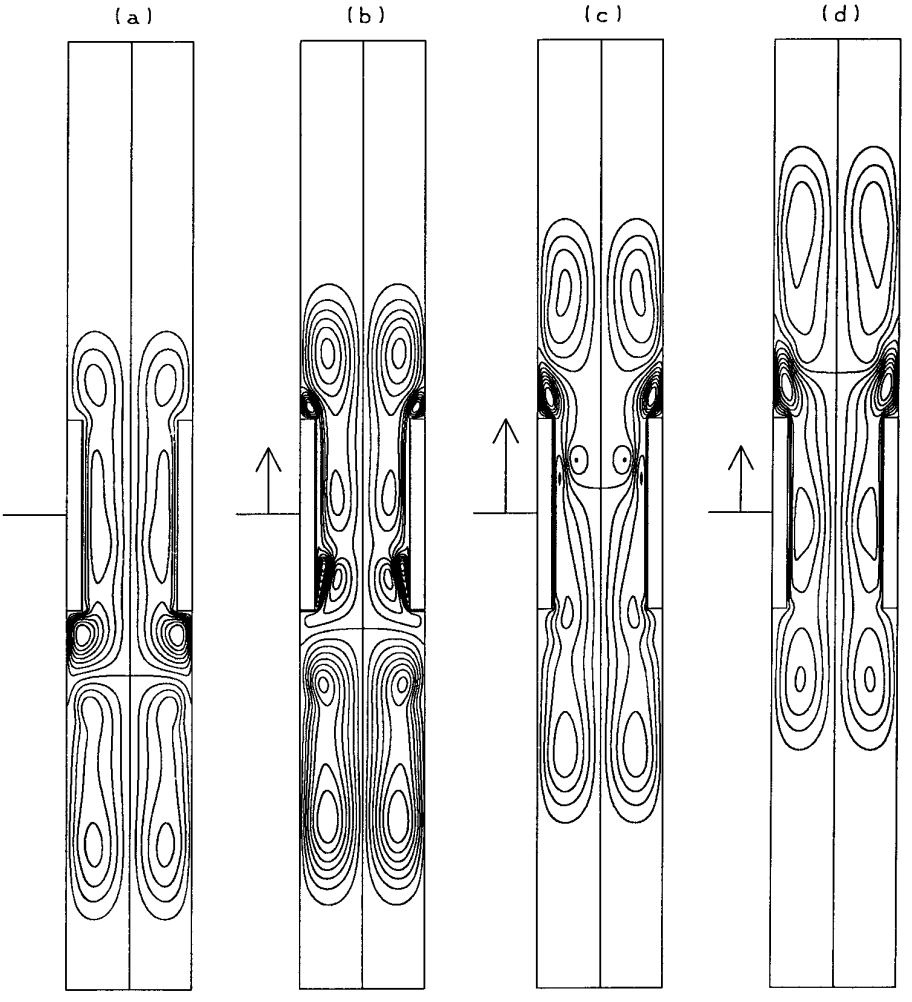

FIG. 10. Evolution of the streamfunction distribution for case 15. Contour plots are generated at (a) $t = 32\pi/4$, (b) $t = 33\pi/4$, (c) $t = 34\pi/4$, and (d) $t = 35\pi/4$.

flow conditions. Thus, R_p is kept almost constant, at the expense of a moderate decrease in the dynamic Reynolds number. Thus, major changes in the dynamics of the vorticity field are not expected, and differences should be essentially attributed to the increase in the boundary layer thickness.

Before discussing the results, we note that the notion of Stokes layer thickness tends to lose its familiar significance as the δ/H becomes as large as 0.4 or 0.6. This is the case because, for high δ/H values, viscous effects affect the entire channel section, and the half-width of the channel, $h/2$, becomes a more appropriate measure of boundary layer thickness. However, we keep referring to δ as Stokes layer thickness, even for cases where Stokes layers cannot develop. (In the latter case, the parameter δ/H is more indicative of the driving frequency or of the plate spacing.) Keeping these issues in mind, we still rely on δ/H parameter in the discussion of computed results, since it naturally derives from the adopted sealing process.

Figures 11 and 12 show that as Re decreases the behavior of the flowfield is dramatically altered. In particular, the impact of flow separation and formation of concentrated vortices is significantly weaker at Re = 574 and 256 than is the case at Re = 2132. Specifically, boundary layer separation at the plate edges at Re = 574 and 256 occurs in a similar fashion to that observed in steady, laminar, sudden-expansion flows. The formation of counterrotating vortices, which was observed in all cases involving the shedding of a thin boundary layer, is barely discernible in Figs. 11 and 12.

The absence of strong counterrotating vortices and the similarity to sudden expansion flows suggest that, for some portions of the acoustic cycle, the flow field on either side of the channel is primarily dominated by one sign of vorticity. Examination of the vorticity field (Fig. 13) reveals that this is in fact the case. However, the flow structure within the channel is quite different from a fully developed pipe flow (Fig. 13d). The boundary layer thickness is very small at one end of the channel, but scales with the channel width at the other end. Thus, the flowfield within the channel is affected by significant spatial and temporal variations in the structure of the boundary layer.

The dependence of flow on Re is further examined by comparing instantaneous velocity profiles across the midsection channel for cases 3 and 17. Figure 14 confirms some of the trends depicted in the streamfunction and vorticity plots. In particular, the thickening of the boundary layers with decreasing Re can be clearly observed. Figure 14 also shows how the increase in the boundary layer thickness leads to a substantial decrease in velocity gradients and, at specific phases, tends to produce profiles that are reminiscent of Poiseuille flow. Another interesting observation is that, due to boundary layer growth and blockage effects, particle velocities within the channel can significantly exceed acoustic speeds in the unobstructed region.

4.5. Effect of Plate Aspect Ratio

Finally, the impact of plate aspect ratio is analyzed. As mentioned above, variation of this stack configuration parameter is implemented by modifying the plate length while keeping other parameters constant (cases 22–27). Examination of computed results (not shown) reveals that, other parameters being equal, there are only minor qualitative variations between stacks with $L/H = 4$ and $L/H = 6.66$. Thus, we limit the discussion to cases 22 and 23, for which streamfunction distributions are plotted in Figs. 15 and 16, respectively.

Comparison of Fig. 15 with Fig. 5 shows interesting differences in flow behavior as the plate aspect ratio is increased from $L/H = 1.32$ to $L/H = 4$. These primarily concern the dynamics of vortex bubbles and recirculation zones within the stack. While the early formation of these structures remains similar to that observed at $L/H = 1.32$, Fig. 15 indicates that the recirculation zones on opposite sides of the channel are no longer anchored at the edges of the plates, but slide along the faces of the plates. These traveling recirculation zones appear to be stuck to the vortex bubble which has formed between them, and the three vortices propagate as a single triple-structure. Due to the increased length of the plate, and since particle displacement parameters are kept constant, this triple vortex structure always remains within the channel.

When the flow reverses, the recirculating zones and vortex bubble first merge and then quickly disappear. Meanwhile, an identical process occurs at the other end of the plates. Obviously, the two processes at different ends of the channel do not occur simultaneously since they are triggered at different phases of flow acceleration. Nonetheless, a decaying vortex triple structure generated at one end (or its remnants) may coexist with a similar younger structure generated at the other.

On the other hand, the behavior of the flow field in the unobstructed region is not significantly affected by the increase in plate length. Comparison of Figs. 15 and 5 indicates that vortex shedding and the subsequent formation of recirculation zones and counterrotating vortex pairs occur in a similar fashion for $L/H = 1.32$ and $L/H = 4$.

Finally, the impact of boundary layer thickness is examined for stack configurations with $L/H = 4$ and 6.66. A sample of the computations is shown in Fig. 16, which shows that decreasing Re substantially affects vortex shedding and internal channel dynamics. In particular, the counterrotating vortex pairs which accompany boundary layer shedding are weak. This is also the case for the vortex structures which form in the channel due to vortex impingement; these structures decay rapidly following their genesis. Thus, the response of the flow to decreasing Re follows the same trends established for stacks with $L/H = 1.32$.

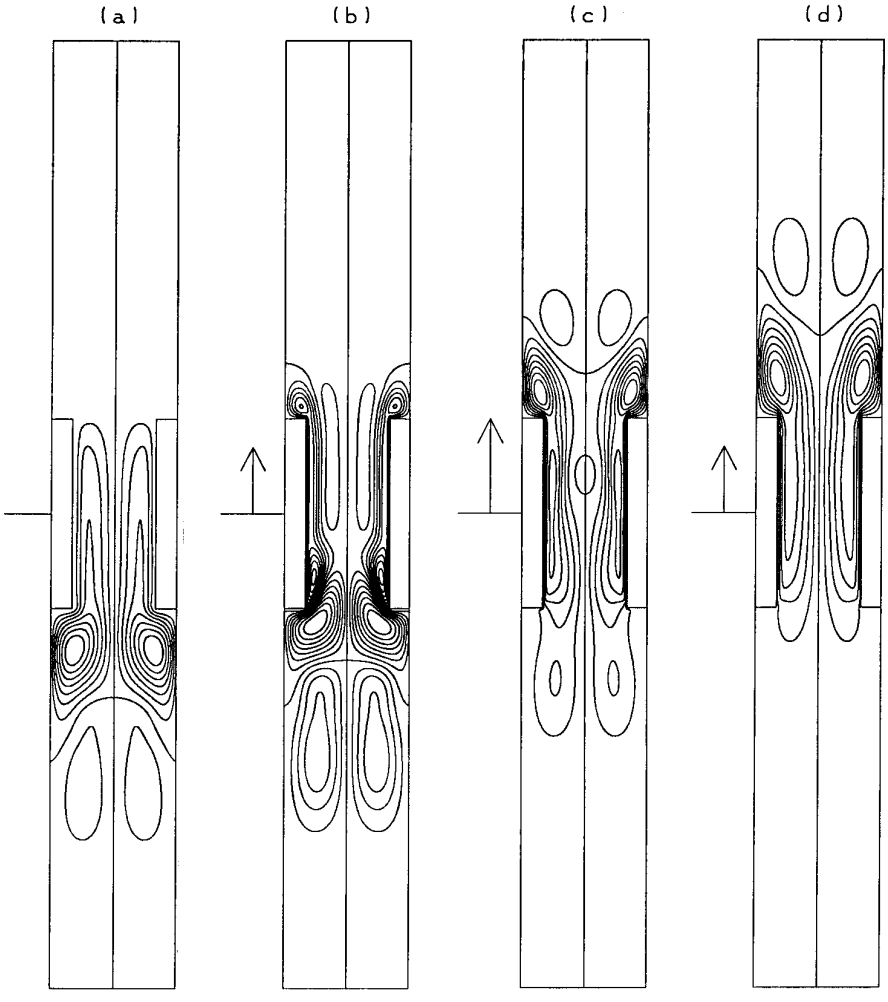

FIG. 11. Evolution of the streamfunction distribution for case 16. Contour plots are generated at (a) $t = 32\pi/4$, (b) $t = 33\pi/4$, (c) $t = 34\pi/4$, and (d) $t = 35\pi/4$.

4.6. Vortex Structures and Energy Losses

Additional insight into the properties of the vortex structures is gained through an abbreviated analysis of (mechanical) energy losses within the stack. These losses are quantified by computing, for each subdomain D^α, $\alpha = \mathrm{I}, \mathrm{II}, \mathrm{III}$, the quantity

$$\Phi_\alpha(t) \equiv \frac{1}{\mathrm{Re}} \int_{D^\alpha} \Theta(x, y, t)\, dV, \tag{4.1}$$

where

$$\Theta(x, y, t) \equiv 2\left\{\left(\frac{\partial u}{\partial x}\right)^2 + \left(\frac{\partial v}{\partial y}\right)^2\right\} + \left(\frac{\partial v}{\partial x} + \frac{\partial u}{\partial y}\right)^2 - \frac{2}{3}\left(\frac{\partial u}{\partial x} + \frac{\partial v}{\partial y}\right)^2 \tag{4.2}$$

is the viscous dissipation function [24]. Thus, $\Phi^\alpha(t)$ is taken as a measure of the total mechanical energy loss occurring in region D^α at time t. We also define a mean energy dissipation rate,

$$\Phi'_\alpha \equiv \frac{1}{|D^\alpha|}\Phi_\alpha, \tag{4.3}$$

where $|D^\alpha|$ is the volume of D^α. We use both Φ and Φ' to examine the impact of unsteady vortex dynamics on energy losses. Computed results for selected cases are shown in Figs. 17 and 18, which respectively illustrate the response of rms values of Φ and Φ' to changes in the normalized Stokes layer thickness, the channel blockage ratio, the stack position, and the plate aspect ratio. The general trends in Figs. 17 and 18 are summarized as follows:

(1) When the stack is located at a velocity antinode,

the mean and total dissipation in domains I and III are identical. This follows immediately from the similarity in the flow structure and its evolution during two half cycles. On the other hand, at $\tilde{k}\tilde{x} = 3\pi/4$ energy losses in domains I and III differ but remain close (Figs. 17c and 18c). This is also expected since the acoustic velocity amplitudes at the matching surfaces differ slightly, due to finite flow-field divergence.

(2) For a short stack ($L/H = 1.32$) energy losses increase with increasing boundary layer thickness (Figs. 17a and 18a). Energy dissipation rates outside the stack and inside the channel are comparable for small boundary layer thickness ($\delta/H = 0.2$), but the former become substantially larger as δ/H increases.

(3) For small boundary layer thickness, $\delta/H = 0.2$, total energy losses in domains I, II, and III appear to be independent of the blockage ratio (Fig. 17b). While this is also the case for the mean energy loss outside the stack (Fig. 18b), the mean energy loss within the stack decreases as the plates are made thinner. This suggests that, in these cases, the total energy loss within the stack is dominated by the contribution of Stokes layers, whose thickness is kept fixed as the blockage ratio is varied.

(4) For $\delta/H = 0.2$, Figs. 17d and 18d indicate that both mean and total energy losses occurring outside the stack are independent of the plate length parameter. This result is not surprising since losses outside the channel result primarily from vortical structures whose evolution is weakly dependent on the plate length. While the mean energy losses within the stack are also independent of L/H, total energy losses in domain II appear to increase linearly with stack length.

While Figs. 17 and 18 undoubtedly contain additional information which may be used to further characterize energy losses, we focus our attention on exploiting the data

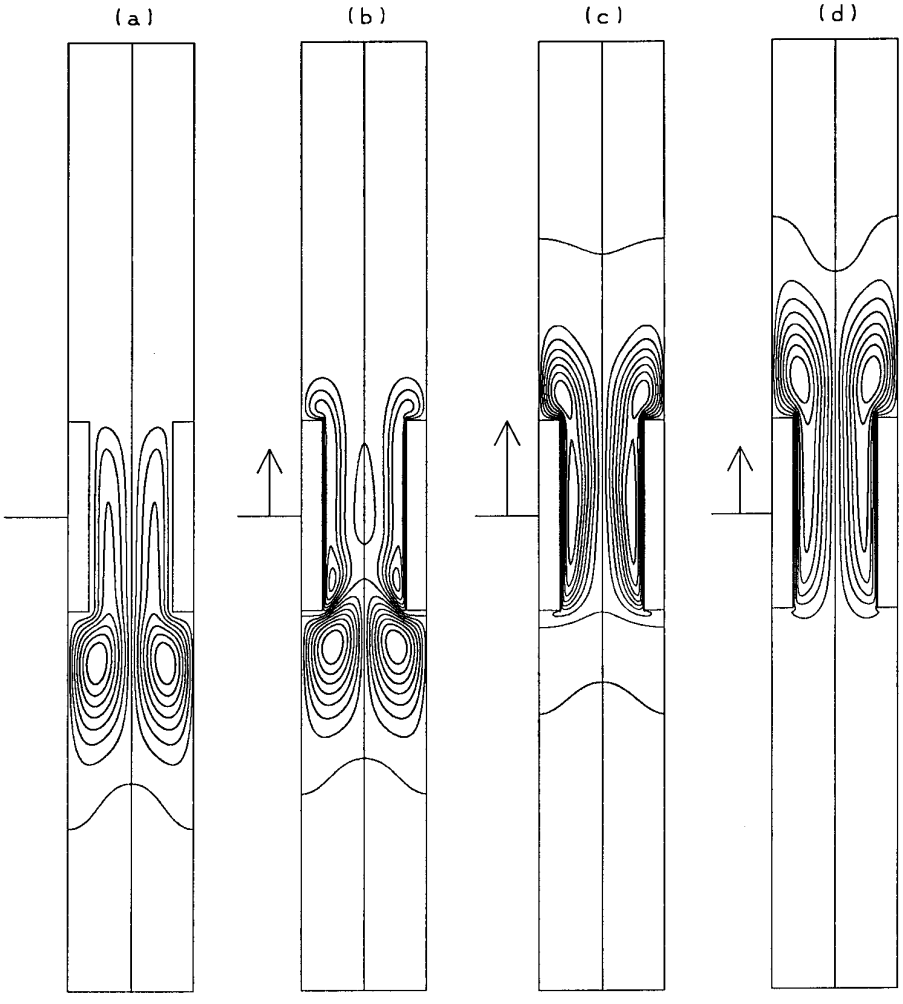

FIG. 12. Evolution of the streamfunction distribution for case 17. Contour plots are generated at (a) $t = 32\pi/4$, (b) $t = 33\pi/4$, (c) $t = 34\pi/4$, and (d) $t = 35\pi/4$.

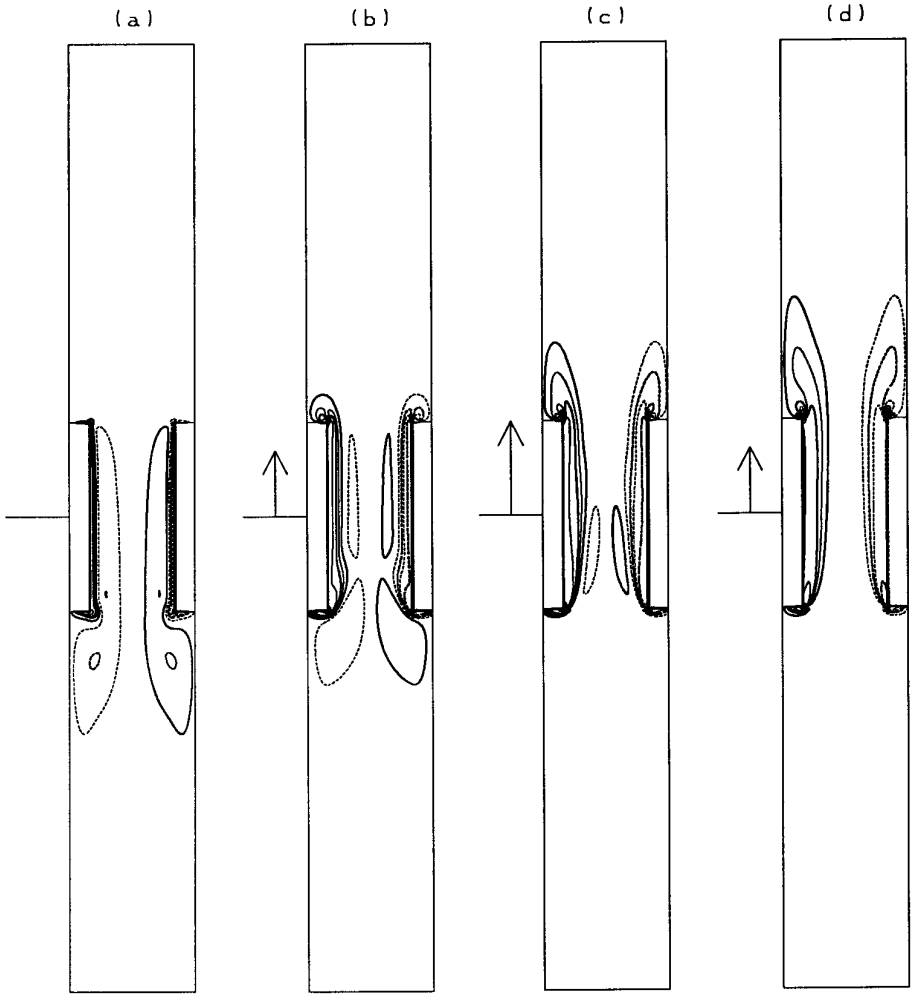

FIG. 13. Evolution of the vorticity field for case 17. Contour plots are generated at (a) $t = 32\pi/4$, (b) $t = 33\pi/4$, (c) $t = 34\pi/4$, and (d) $t = 35\pi/4$.

to examine the validity of some scaling relationships which are motivated by our observations in Sections 4.1–4.5. For brevity, we restrict the present exercise to the cases of Fig. 17a.

We start with a simple scaling expression for the dimensional total energy dissipation with a region of the flow. Following Eq. (4.1), we postulate

$$\tilde{\Phi} \sim \tilde{\mu} \left(\frac{\tilde{V}_c}{\tilde{l}_c} \right)^2 \tilde{\vartheta}_c, \tag{4.4}$$

where $\tilde{\mu}$ is the dimensional dynamic viscosity, $\tilde{V}_c$ is a characteristic velocity difference, $\tilde{l}_c$ is a characteristic length and

$$\tilde{\vartheta}_c \sim \tilde{\chi}\tilde{\hbar} \tag{4.5}$$

is the characteristic volume (in 2D).

Within the stack (domain II), the analysis provided above suggests the following order-of-magnitude estimates: (a) $\tilde{V}_c \sim \tilde{u}_a$, the acoustic velocity. This is justified because the blockage ratio is kept constant. (b) $\tilde{l}_c \sim \tilde{\delta}$, the Stokes layer thickness. This approximation is expected to remain valid as long as $\tilde{\delta}$ does not significantly exceed the channel half-width. (c) Following the argument just provided we use $\tilde{\hbar} \sim \tilde{\delta}$, and $\tilde{\chi} \sim \tilde{L}$, the channel length. Performing these substitutions, normalizing the resulting expression, and ignoring dimensionless groups that are kept fixed yields the hypothesis

$$\Phi^{\mathrm{II}} \propto \frac{R_p^3}{\mathrm{Re}_a} \tag{4.6}$$

Meanwhile, the flow visualization experiments in Section 4.1 suggest a different scaling for characteristic lengths outside the stack (regions I and III). While the acoustic speed is still used characteristic velocity $\tilde{V}_c \sim \tilde{u}_a$, the plate

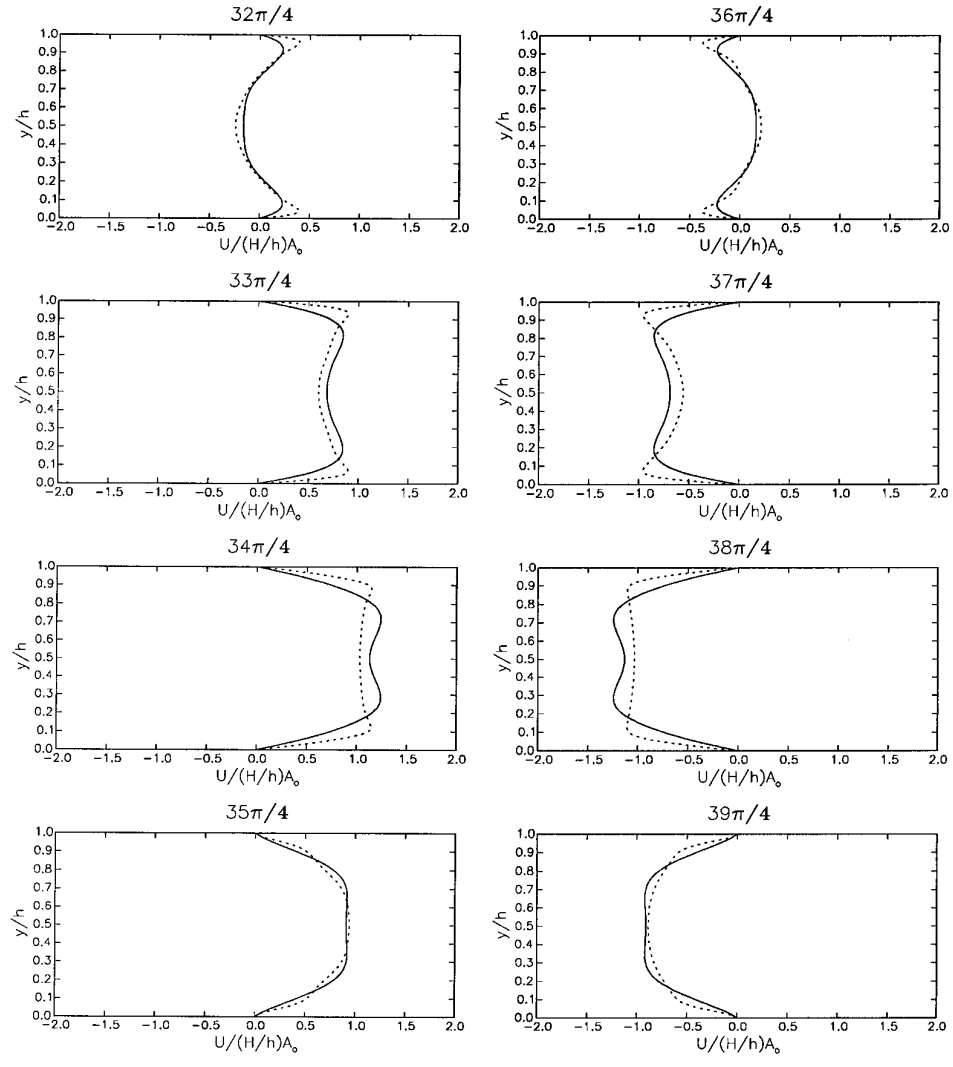

FIG. 14. Profiles of normalized instantaneous streamwise velocity across the midsection of the channel, for cases 17 (———) and 3 (– – –). The streamwise velocity is normalized using the acoustic amplitude at the matching surface and the channel blockage ratio. Times corresponding to different frames are indicated.

thickness $\tilde{d}$ is used both in the estimate of the velocity gradient and as a measure of the height of the region contributing to the energy dissipation. We thus use $\tilde{l}_c \sim \tilde{d}$ and $\hbar \sim \tilde{d}$. Finally, $\aleph$ is scaled using an estimate for the length of the separated flow zone at the plate edge. Since the length of this vortical region is expected to scale with particle velocities, we use $\aleph \sim \tilde{u}_a/\tilde{\Omega}$. Substituting these estimates and normalizing, we obtain the scaling relationship

$$\left.\begin{matrix}\Phi^{\mathrm{I}} \\ \Phi^{\mathrm{III}}\end{matrix}\right\} \propto \frac{R_p^5}{\mathrm{Re}_a^2} \tag{4.7}$$

To test the validity of estimates (4.6) and (4.7), we plot in Figs. 19 and 20 two scaled versions of the total dissipation, $\Phi\ \mathrm{Re}_a/R_p^3$ and $\Phi\ \mathrm{Re}_a^2/R_p^5$, respectively, for the same conditions of Figs. 17a. Figure 19 clearly shows that within the channel (domain II) the scaled energy dissipation $\Phi\ \mathrm{Re}_a/R_p^3$ is essentially independent of the imposed changes to δ/H. Figure 20 also shows that in domains I and III the curve for $\Phi\ \mathrm{Re}_a^2/R_p^5$ is almost flat. Thus, these results further support scaling relationships given above.

4.7. Computational Perspectives

While the constructions in Section 3 appear fairly simple, implementation of the resulting numerical schemes reveals a number of delicate computational issues which deserve further discussion. These primarily concern selection of

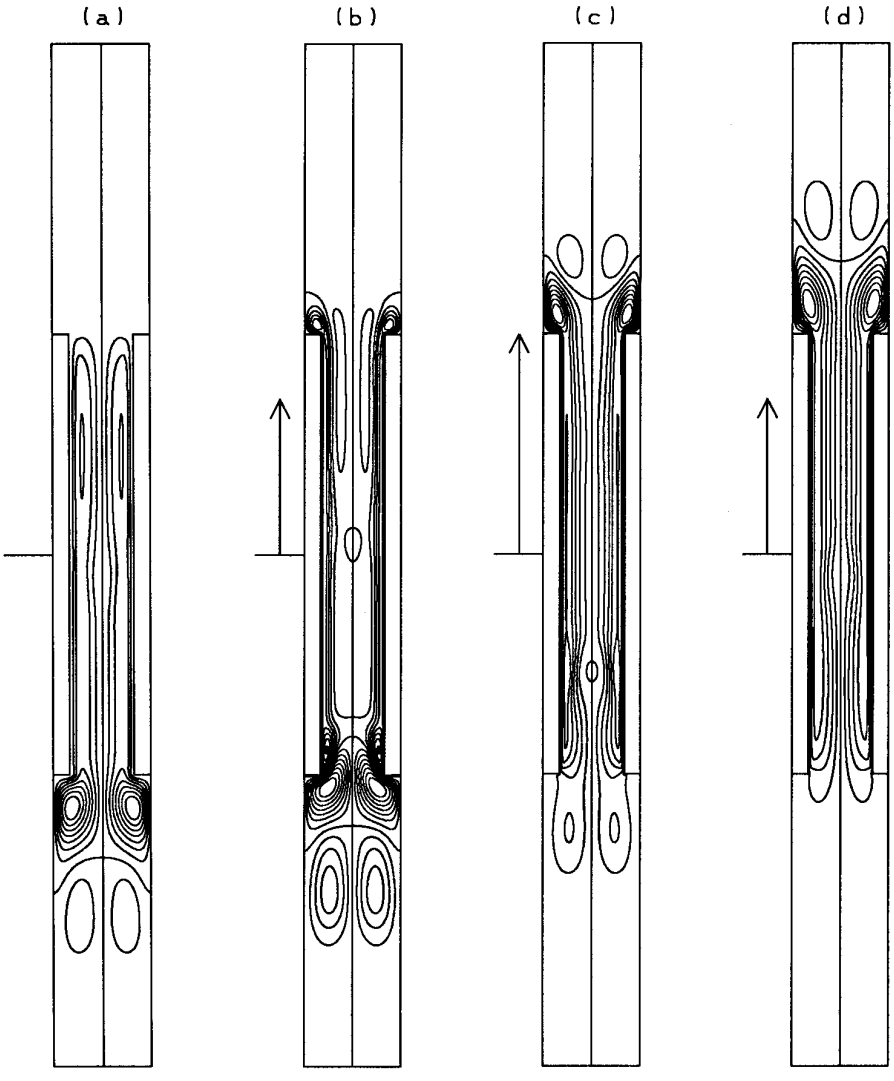

FIG. 15. Evolution of the streamfunction distribution for case 22. Contour plots are generated at (a) $t = 32\pi/4$, (b) $t = 33\pi/4$, (c) $t = 34\pi/4$, and (d) $t = 35\pi/4$.

vorticity and streamfunction boundary conditions on matching surfaces and of the location of these surfaces. Other noteworthy items include vorticity boundary conditions on solid surfaces and the validity and performance of the domain decomposition/boundary Green's function/fast solver version of the computations. Comments on each of these issues are provided below.

Analysis of the impact of boundary conditions is based on comparing predictions of several variants of the computations. Variants are distinguished according to means of imposing vorticity boundary conditions on solid surfaces and according to vorticity and streamfunction boundary conditions on matching surfaces. As indicated in Section 3, while vorticity boundary conditions on solid surfaces ''derive'' from the requirement of a vanishing slip velocity, a large number of possibilities exist for matching surfaces, several of which were included in the numerical study (Table II). Variants are tested within codes which rely on direct matrix inversion solvers; i.e., the numerical study of boundary conditions is carred out independently of the development of the domain decomposition/fast solver.

While the numerical study gave results that are consistent with well-established experiences on the application of finite-difference techniques (e.g., [20, 26, 27]), several issues were also addressed, as summarized below (see Table II):

(1) For fixed mesh size and fixed location of the acoustic matching boundaries, all variants yield nearly identical results when the drive ratio, Dr, is small. However, as Dr is increased, schemes 1–4 show signs of numerical instability, while scheme 5 remains stable. The ''robustness'' of

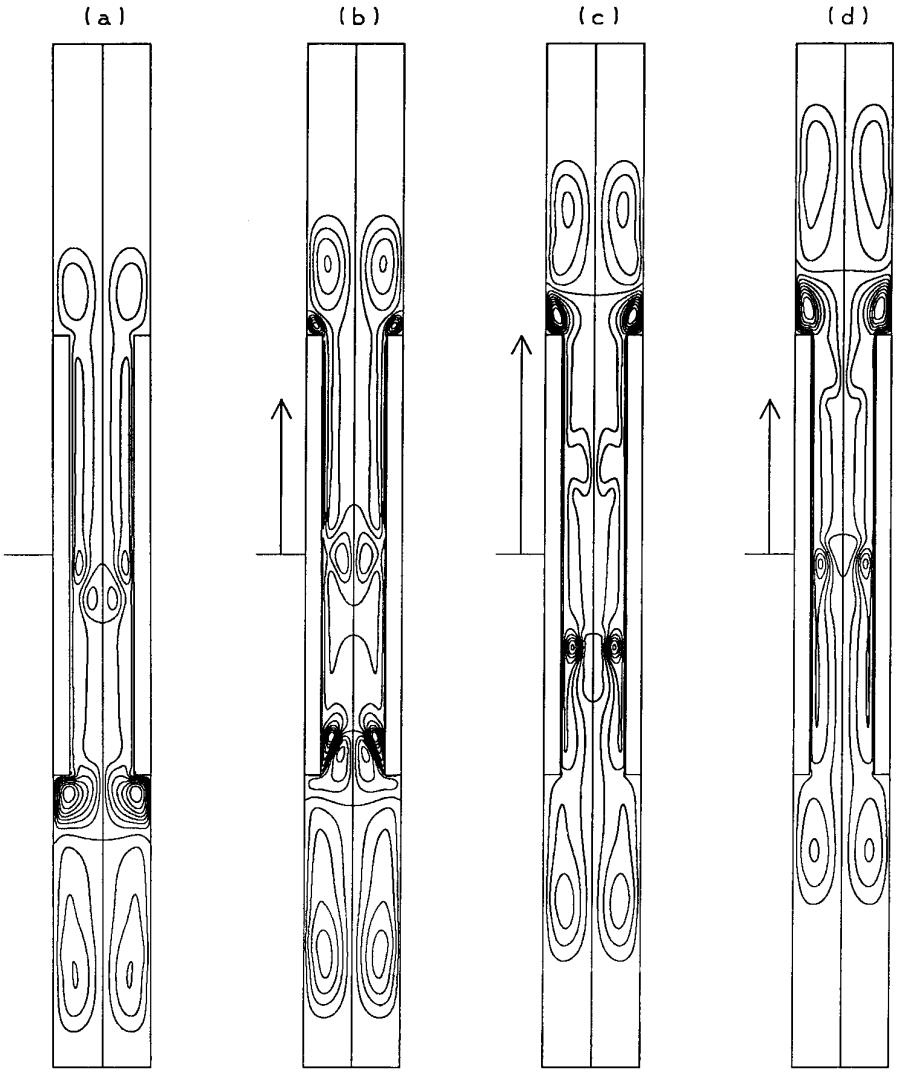

FIG. 16. Evolution of the streamfunction distribution for case 23. Contour plots are generated at (a) $t = 32\pi/4$, (b) $t = 33\pi/4$, (c) $t = 34\pi/4$, and (d) $t = 35\pi/4$.

scheme 5 is the primary reason behind its selection in the computations above.

(2) For the present selection of numerical parameters (Table I), vorticity boundary conditions at solid surfaces have little impact on computed results. Briefly, results obtained with first- and second-order approximations of vorticity boundary conditions at solid surfaces exhibited small differences. This result is not surprising since, in all computations, the grid Reynolds number is small; a limited convergence analysis enabled us to verify that this also leads to a very weak dependence of the results on the mesh size. We also find that implementation of different vorticity boundary conditions on solid surfaces has no impact on the occurrence of the numerical instability mentioned above.

(3) The origin of the numerical instability observed in the present study can be traced to the selection and implementation of vorticity and streamfunction conditions on acoustic matching surfaces and to the location of these surfaces. The instability primarily occurs in the form of blowup of the vorticity at the matching surfaces, when derivative conditions on vorticity are used, or close to the matching surfaces, when homogeneous Dirichlet boundary conditions on vorticity are imposed.

(4) Detailed examination of this phenomenon shows that the numerical instability occurs when vorticity generated at solid boundaries migrates towards the matching surfaces and tends to cross them. This observation is consistent with our earlier observation that all schemes are stable at low drive ratio, in which case the vortices tend to be confined to a small neighborhood of the plates. With the

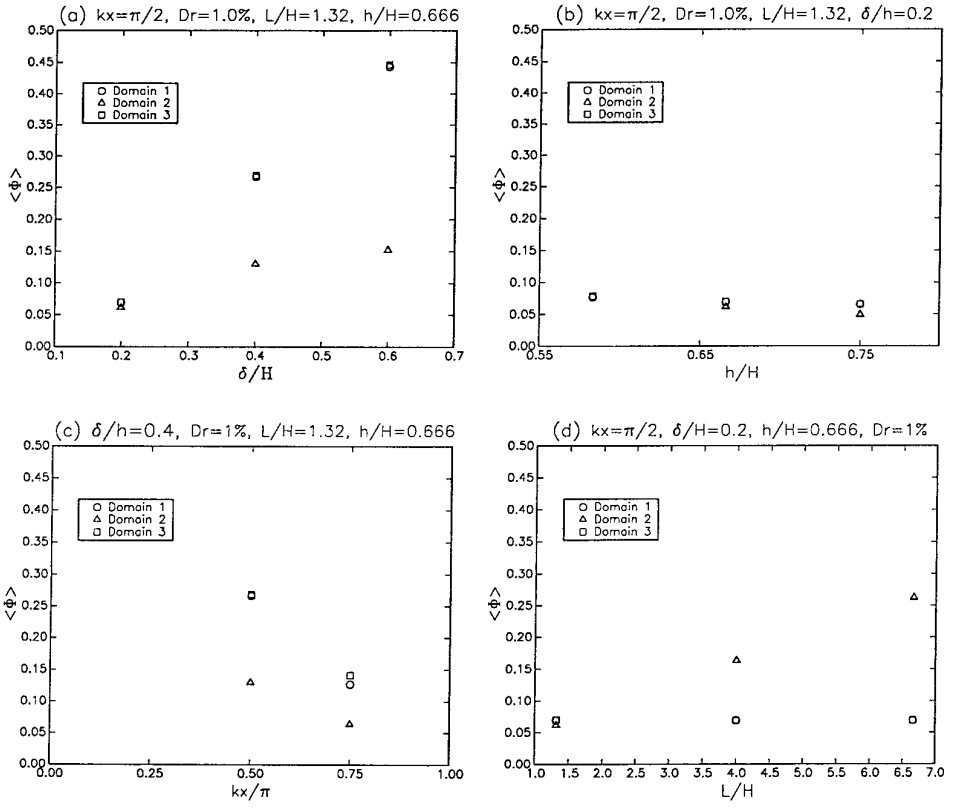

FIG. 17. Dependence of the total dissipation, Φ, on: (a) the normalized Stokes layer thickness (cases 3, 16, 17); (b) the blockage ratio (cases, 3, 9, 15); (c) the stack position (cases 16, 18); and (d) the plate aspect ratio (cases 3, 22, 25).

increase in drive ratio, particle displacements also increase, thus triggering the numerical instability. The problem may be circumvented by extending regions I and III, at the expense of an increase in computational cost.

(5) While several means for overcoming this difficulty may be conceived—possibly by ensuring fine resolution of thin vortical structures associated with impingement of vorticity on matching surfaces—we have opted not to pursue such alternatives. Rather, the more stable and accurate variant 5a is adopted *while* ensuring that matching surfaces are sufficiently removed from the solid plates.

While, as mentioned earlier, schemes 5 remain stable even when vorticity crosses matching surfaces, the location of these surfaces is still observed to have some effect on the computations. Briefly, as long as the matching surfaces are not placed very close to the plates, the broad features of the flow and vorticity fields are insensitive to the location of surfaces. This further motivates the selection of strong/inflow weak/outflow vorticity boundary conditions.

(6) However, even the large-scale features of the flow are essentially independent of the position of matching surfaces; the results still exhibit strong sensitivity to the location of these surfaces whenever strong vorticity crosses them. To illustrate this claim, we compute the pressure drop across the stack using the general force balance for a control volume D enclosed by a surface S,

$$\frac{\partial}{\partial t}\int_D \rho u_i \, dV = -\int_S [\rho u_i n_j u_j + p n_i - n_j \tau_{ij}] \, dA. \quad (4.8)$$

Here, $\mathbf{n}$ is the outer normal to the surface while τ_{ij} is the shear stress tensor. Equation (4.8) is applied to five subregions of the computational domain, as shown in Fig. 21. We arbitrarily fix a mean pressure value and use the integral momentum balance relationships to determine the unknown pressures: p_{AB}, p_{CD}, p_{EF}, p_{GH}, p_{IJ}, p_{KL}, and, consequently, the net pressure force acting across the stack, $p_{AB} - p_{GH}$.

An example of pressure force computations is given in Figs. 22 and 23, which show predictions of unsteady pressure difference across the stack for two different discretizations. Figure 22 shows the predictions for case 3 (Table I). Meanwhile, Fig. 23 is obtained for the same "physical" conditions, mesh size, and time step as case 3; however, the matching surfaces have been moved closer towards the plates by reducing, in domains I and III, the number of elements along the x-direction.

While Figs. 22 and 23 show several differences in the

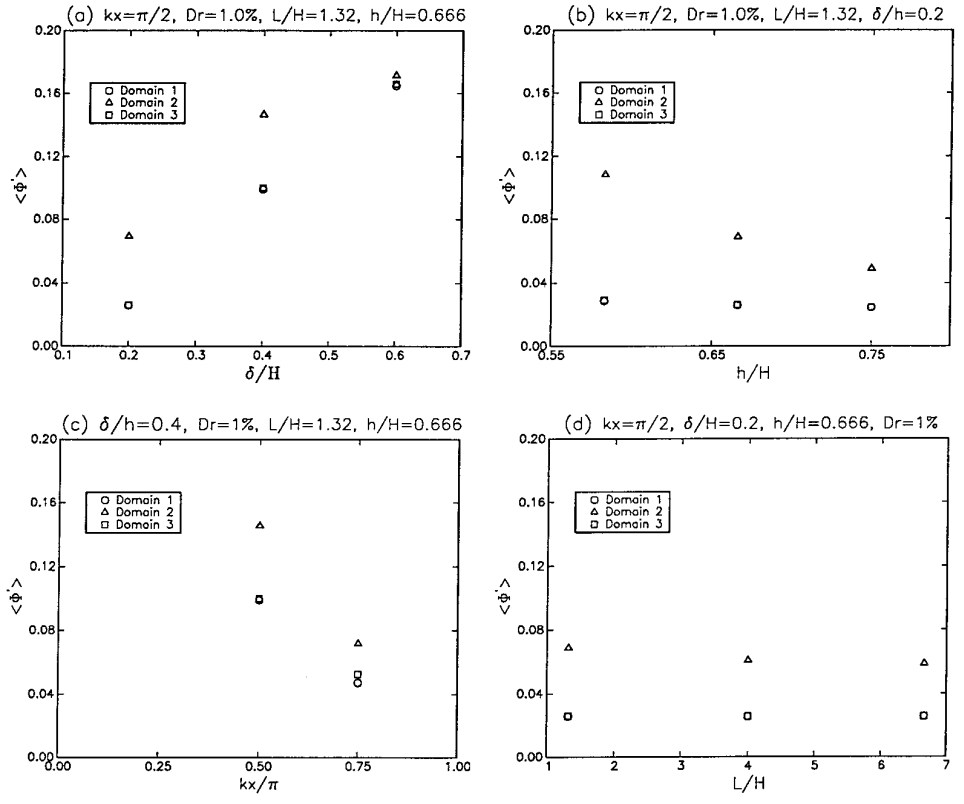

FIG. 18. Dependence of the mean dissipation, Φ', on: (a) the normalized Stokes layer thickness (cases 3, 16, 17); (b) the blockage ratio (cases, 3, 9, 15); (c) the stack position (cases 16, 18); and (d) the plate aspect ratio (cases 3, 22, 25).

corresponding pressure curves, a disturbing observation is the saw-tooth shape and lack of symmetry in the curve of Fig. 23. The origin of the behavior of Fig. 23 can also be traced to migration of strong vorticity towards acoustic matching surfaces. This claim is based on detailed comparison (not shown) of the predictions of Fig. 22 to results obtained at lower drive ratios and to results obtained for the same drive ratio but for larger separation between the plates and the matching surfaces. In these situations, i.e., when the matching surfaces remain essentially vorticity-

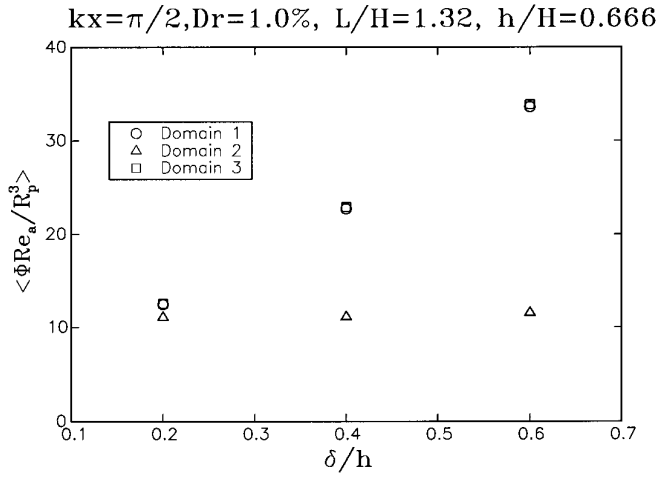

FIG. 19. Scaled total dissipation, $\Phi\ \mathrm{Re}_a/R_p^3$, for the same cases of Fig. 17a.

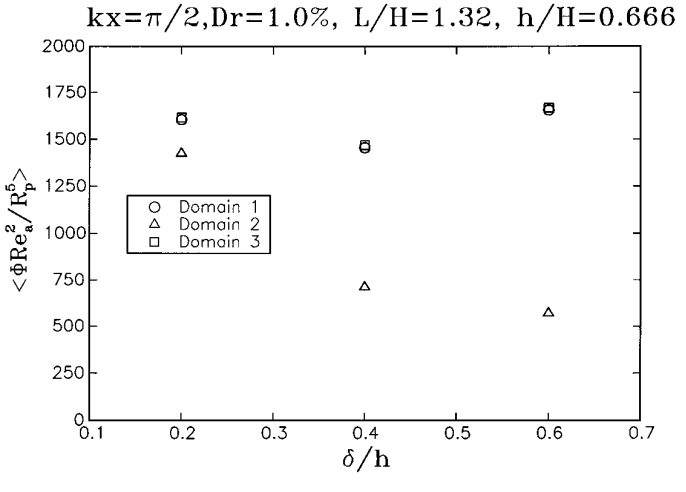

FIG. 20. Scaled total dissipation, $\Phi\ \mathrm{Re}_a^2/R_p^5$, for the same cases of Fig. 17a.

TABLE II

Vorticity and Streamfunction Boundary Conditions

Scheme	Streamfunction: Matching surface	Vorticity: Solid surface	Vorticity: "Inflow"	Vorticity: "Outflow"
1a	$\psi = 0$	$\frac{\partial \psi}{\partial n} = \pm u_s$ (II)	$\frac{\partial \psi}{\partial x} = \nu_s$ (II)	$\frac{\partial \psi}{\partial x} = \nu_s$ (II)
1b	$\psi = 0$	$\frac{\partial \psi}{\partial n} = \pm u_s$ (II)	$\frac{\partial \psi}{\partial x} = \nu_s$ (I)	$\frac{\partial \psi}{\partial x} = \nu_s$ (I)
1c	$\psi = 0$	$\frac{\partial \psi}{\partial n} = \pm u_s$ (I)	$\frac{\partial \psi}{\partial x} = \nu_s$ (I)	$\frac{\partial \psi}{\partial x} = \nu_s$ (I)
2a	$\frac{\partial \psi}{\partial x} = \nu_s$	$\frac{\partial \psi}{\partial n} = \pm u_s$ (II)	$\omega = 0$	$\omega = 0$
2b	$\frac{\partial \psi}{\partial x} = \nu_s$	$\frac{\partial \psi}{\partial n} = \pm u_s$ (I)	$\omega = 0$	$\omega = 0$
3a	$\frac{\partial \psi}{\partial x} = 0$	$\frac{\partial \psi}{\partial n} = \pm u_s$ (II)	$\omega = 0$	$\omega = 0$
3b	$\frac{\partial \psi}{\partial x} = 0$	$\frac{\partial \psi}{\partial n} = \pm u_s$ (I)	$\omega = 0$	$\omega = 0$
4a	$\psi = 0$ inflow; $\frac{\partial \psi}{\partial x} = 0$ outflow (I)	$\frac{\partial \psi}{\partial n} = \pm u_s$ (II)	$\frac{\partial \psi}{\partial x} = \nu_s$ (II)	$\frac{\partial \psi}{\partial x} = \nu_s$ (II)
4b	$\psi = 0$ inflow; $\frac{\partial \psi}{\partial x} = 0$ outflow (I)	$\frac{\partial \psi}{\partial n} = \pm u_s$ (II)	$\frac{\partial \psi}{\partial x} = \nu_s$ (I)	$\frac{\partial \psi}{\partial x} = \nu_s$ (I)
4c	$\psi = 0$ inflow; $\frac{\partial \psi}{\partial x} = 0$ outflow (I)	$\frac{\partial \psi}{\partial n} = \pm u_s$ (I)	$\frac{\partial \psi}{\partial x} = \nu_s$ (I)	$\frac{\partial \psi}{\partial x} = \nu_s$ (I)
5a	$\psi = 0$	$\frac{\partial \psi}{\partial n} = \pm u_s$ (II)	$\omega = 0$	$\frac{\partial \omega}{\partial x} = 0$ (II)
5b	$\psi = 0$	$\frac{\partial \psi}{\partial n} = \pm u_s$ (I)	$\omega = 0$	$\frac{\partial \omega}{\partial x} = 0$ (II)

(I). First-order treatment of Neumann boundary conditions.
(II). Second-order treatment of Neumann boundary conditions.

free, we find that pressure signals follow essentially the same shape and exhibit similar behavior during acoustic half-cycles. Consequently, although the matching surfaces may not affect the stability of the computations nor prediction of large-scale flow features, it still appears important that matching surfaces remain sufficiently removed from the solid boundaries.

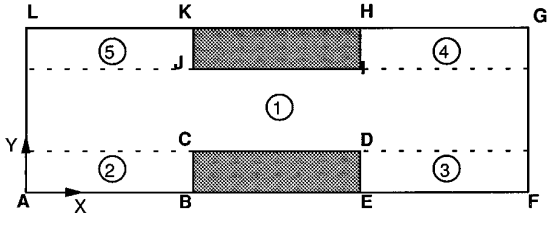

FIG. 21. Schematic illustration of the computational domain showing the definition of surfaces and subregions for momentum integral computations.

(7) In an attempt to limit the computational overhead by keeping the computational domain as short as possible, we have further analyzed the pressure behavior observed in Fig. 23. Specifically, assuming that it may be of a "transient" nature, we have considered the possibility that the ("anomalous") pressure behavior may be "cured" if the computations are extended over additional cycles. However, we find that the curve in Fig. 23 simply repeats itself essentially unchanged for 12 additional cycles. It thus appears that the pressure signal is essentially locked into the behavior mode depicted in the plots.

Hypothesizing that the pressure behavior in Fig. 23 may be related to the startup procedure used in the computations, we have also examined the effects of (a) initializing the computations using "time-periodic" results obtained

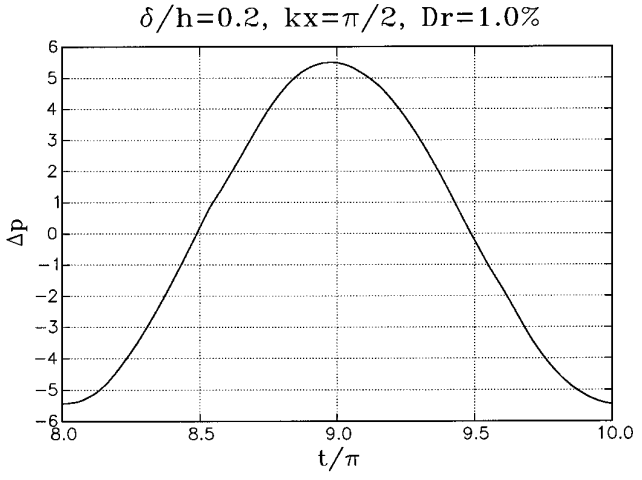

FIG. 22. Evolution of the pressure difference across the stack in case 3. The matching surfaces are at a distance 2.64*H* from the plates.

at lower drive ratio and (b) using a smooth initial increase in the acoustic pressure amplitude. However, we find that (1) the startup procedure has only a minute effect on the predictions when vorticity crosses matching surfaces and (2) the final stages of the simulation are independent of the initial conditions when matching surfaces are appropriately located.

We conclude this section with brief comments on the domain decomposition/fast solver version of the computations. Based on tests conducted at both low and high drive ratios, nearly identical results are obtained using the direct matrix scheme and the domain decomposition/fast solver. The advantage of the latter approach is that it yields significant savings in memory and CPU requirements. For instance, for the conditions of case 3 (Table I), memory requirements are reduced from approximately 13 Megawords (Mw) to 2 Mw on the CRAY C90. This is a significant reduction since the direct inversion technique relies on a banded storage of system matrices. In addition, significant reduction in CPU requirement of the velocity inversion routine, which accounts for most of the computational overhead is also achieved. For the conditions of case 3, the velocity inversion routine requires 0.381 s (at 120 Mflops) for the direct solver, while only 0.015 s (at 424 Mflops) is needed by the fast solver. Thus, the fast solver is roughly 25 times more efficient than the direct solver.

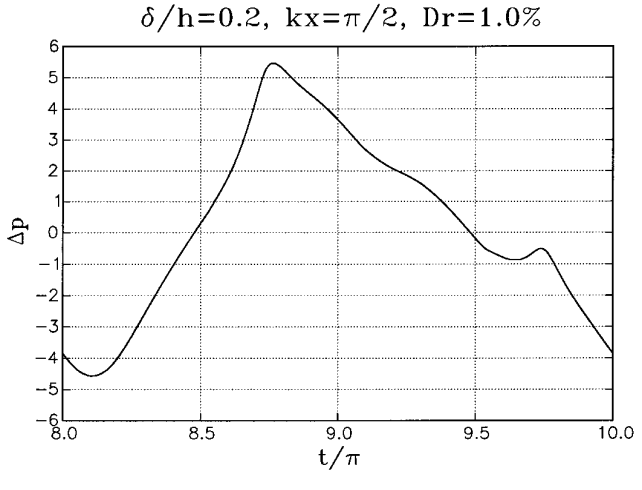

FIG. 23. Evolution of the pressure difference across the stack, using the same mesh size and time step as case 3. The matching surfaces are at a distance 1.32*H* from the plates.

5. SUMMARY AND CONCLUSIONS

This paper describes the development of a low Mach-number model for simulation of unsteady flow in a thermoacoustic stack. It is based on an a quasi-1D idealization of the action of acoustic standing waves and detailed 2D resolution of flow phenomena occurring in a neighborhood of the thermoacoustic stack. The approximation relies on a low Mach-number limit of the governing equations which enables us to ignore wave motion within the stack while still retaining leading-order compressibility effects. In addition, a simplified representation of acoustic standing wave, in terms of unsteady velocity boundary conditions, is incorporated. This development enables us to overcome the stiff scale complexity of the problem, which is characterized by large disparity between acoustic wavelength, stack dimension, and relevant viscous and dynamical lengthscales. In its current form, the model is restricted to situations where stratification effects are weak, namely to stacks operating at low drive ratio.

A vorticity-based simulation scheme of the governing equations is constructed. The scheme relies on the Helmholtz decomposition of the velocity vector into an irrotational and divergence-free component. Evolution of the irrotational component follows that of the imposed acoustic standing wave. Meanwhile, evolution of the divergence-free velocity component is found by integrating the vorticity transport equation and inverting the vorticity streamfunction Poisson equation. Time integration is performed using a third-order accurate scheme, while spatial discretization is based on second-order finite differences.

Two different means of inverting the streamfunction Poisson equation, which accounts for most of the CPU, are developed. The first is based on an unpivoted Gaussian elimination routine which is applied to perform an LU decomposition of the system matrix. The second exploits the special geometry of the stack by developing a domain decomposition/Green's function approach. By relying on Fourier methods in the inversion process, the domain decomposition scheme achieves a large reduction in memory

requirements and order-of-magnitude speedup of the computations.

The latter variant is applied to the examine the essential features of flow and vorticity fields in the neighborhood of a thermoacoustic stack. It is shown that evolution of the flowfield is strongly modulated by the motion of complex vortical structures which form due to the shedding of Stokes layers and by the impingement of these structures on the edges of the stack. The response of this motion to changes in flow and stack configuration parameters is also analyzed.

As mentioned earlier, the current implementation of the computational model suffers from two primary restrictions. The first concerns the assumption of weak stratification effects. This assumption may be immediately relaxed simply by restoring the general form of the low Mach-number energy and vorticity transport equations. However, this extension would require a careful analysis of temperature boundary conditions.

The second limitation of the present model, which has prompted us to postpone the extension mentioned above, is that it also simplifies acoustics–vorticity interactions. Since the response of the stack is expected to reflect a strong coupling between the motion of concentrated eddies close to solid boundaries and the acoustic waves within the resonance tube, it is felt that extension of the model to account for such coupling should be first conducted. Effort is currently underway to couple the present methodology with a more general low Mach-number asymptotic analysis [28] which appears ideally suited for this task.

ACKNOWLEDGMENTS

This work is supported by the Office of Naval Research. Computations were performed at the Pittsburgh Supercomputer Center. Helpful discussions with Professors R. Klein, A. Prosperetti, and C. Herman are also acknowledged.

REFERENCES

1. Lord Rayleigh, *Theory of Sound* (Dover, New York 1945).
2. N. Rott, in *Adv. Appl. Mech.* **20,** 135 (1980).
3. A. A. Atchley, H. E. Bass, T. J. Hofler, and H. T. Lin, *J. Acoust. Soc. Am.* **91,** 734 (1992).
4. A. A. Atchley, *J. Acoust. Soc. Am.* **92,** 2907 (1992).
5. J. Wheatley, T. Hofler, G. W. Swift, and A. Migliori, *J. Acoust. Soc. Am.* **74,** 153 (1983).
6. G. W. Swift, *J. Acoust. Soc. Am.* **84,** 1145 (1988).
7. N. Rott, *J. Appl. Math. Phys.* **25,** 619 (1974).
8. A. A. Atchley, T. J. Hofler, M. L. Muzzerall, M. D. Kite, and C. Ao, *J. Acoust. Soc. Am.* **88,** 251 (1990).
9. T. J. Hofler, Ph.D. thesis, Physics Department, University of California at San Diego, 1986 (unpublished).
10. P. Merkli and H. Thomann, *J. Fluid Mech.* **70,** 161 (1975).
11. G. W. Swift and R. M. Keolian, *J. Acoust. Soc. Am.* **94,** 941 (1993).
12. W. P. Arnott, H. E. Bass, and R. Raspet, *J. Acoust. Soc. Am.* **90,** 3228 (1991).
13. R. L. Panton, *Incompressible Flow* (Wiley, New York, 1984).
14. A. Majda and J. Sethian, *Combust. Sci. Technol.* **42,** 185 (1985).
15. A. F. Ghoneim and O. M. Knio, in *Twenty First Symposium* (*International*) *on Combustion, The Combustion Institute, 1986,* p. 1313.
16. Ghoniem, A. F., in *Lectures in Applied Mathematics,* Vol 24, Am. Math. Soc., Providence, RI, (1985), p. 199.
17. P. A. McMurty, W. H. Jou, J. J. Riley, and R. W. Metcalfe, *AIAA J.* **24,** 962 (1986).
18. J. R. Olson and G. W. Swift, *J. Acoust. Soc. Am.* **95,** 1405 (1994).
19. P. Merkli and H. Thomann, *J. Fluid Mech.* **68,** 567 (1975).
20. C. A. J. Fletcher, *Computational Techniques for Fluid Dynamics* (Springer-Verlag, New York, 1987).
21. O. Daube, *J. Comput. Phys.* **103,** 402 (1992).
22. C. Hirsch, *Numerical Computation of Internal and External Flows* (Wiley, New York, 1989).
23. D. Anderson, J. Tannehill, and R. Pletcher, *Computational Fluid Mechanics and Heart Transfer* (Hemisphere, New York, 1984).
24. H. Schlichting, *Boundary Layer Theory* (McGraw–Hill, New York, 1987).
25. A. S. Worlikar, M.S. thesis, Department of Mechanical Engineering, The Johns Hopkins University, 1995, (unpublished).
26. R. Peyret and T. D. Taylor, *Computational Methods for Fluid Flow* (Springer-Verlag, New York, 1983).
27. M. M. Gupta and R. P. Manohar, *J. Comput. Phys.* **31,** 265 (1979).
28. R. Klein, *J. Comput. Phys.* **121,** 213 (1995).